JOURNAL OF COMPUTATIONAL PHYSICS 119, 1–25 (1995)

Robust Multigrid Solution of the Shallow-Water Balance Equations*

IRAD YAVNEH† AND JAMES C. MCWILLIAMS

National Center for Atmospheric Research, Boulder, Colorado 80307-3000

Received December 11, 1992; revised September 2, 1994

Balance Equation models describing accurate, gravity-wave-free states on the so-called "slow manifold" of the Primitive Equations are of wide and growing interest, both theoretical and practical, for geophysical fluid dynamics. As a particular example with only two spatial dimensions, the Shallow-Water Balance Equations are a coupled, highly nonlinear, nonsymmetric system of partial differential equations, for which only *ad hoc* solvers of limited robustness have previously been developed. Two multigrid algorithms are presented, one explicit and one implicit in time, which are shown by analysis and numerical examples to be efficient and robust solution techniques for this system. These examples include modons and Shallow-Water turbulence at finite Rossby number. It is found that, in some regimes of physical parameters, quite large time steps can be taken with the implicit solver, with little loss of accuracy or efficiency. This is interpreted as due to significantly slower evolutionary rates of the dominant patterns compared to parcel trajectory rates.

1. INTRODUCTION

Fluid motions on scales of kilometers and larger in the earth's oceans and atmosphere are typically highly anisotropic in velocity due to the influences of stable stratification and planetary rotation. Partly in consequence, they also have evolutionary rates principally set by either advection or planetary-wave motion (i.e., Rossby waves). In this sense these motions reside on the slow manifold in the phase space of all motions admitted by the fundamental equations, and other possible modes with faster rates—such as acoustic, gravitational, and inertial waves—usually have both relatively small amplitudes and weak dynamical coupling to slow modes. The self-consistent dynamics of the slow manifold is generally referred to as balanced dynamics, and particular sets of equations have been shown to be quite accurate relative to the slowly evolving solution components of the more fundamental equations; examples of such systems are, respectively, the Balance Equations ([7, 17, 12, 13]) and the hydrostatic Primitive Equations, which are the usual basis for weather-prediction and climate models.

We are interested in computational methods for solving these equations in order to investigate the dynamics of the slow manifold. The Balance Equations, as a concomitant to the exclusion of the fast wave modes through reduction of the temporal order, are uniquely challenging to integrate as a PDE system because their temporal derivatives cannot be evaluated from closed-form expressions, but rather must be solved for implicitly. The methods employed to date (e.g., [1, 20]) have used simple relaxation-iteration methods to resolve this implicitness, and it has also been found to be efficacious to blend this iteration with a predictor-corrector time-stepping iteration. The degree of temporal-derivative implicitness is asymptotically small in either a Rossby or Froude number (R and F are defined in Section 2), but these simple iterative methods experience severe slowing down of convergence (or failure) when the implicitness is sufficiently large. Thus, we seek solution methods which will allow us to increase the scope of our investigation to include regimes of relatively large R and F (more precisely, the corresponding local parameters R' and F' defined in (56–57)), which are intractable by previous methods. This is necessary in particular when the fluid-height in some part of the domain is small compared to the average height (see [30], where the present method is used in studying such regimes).

Multigrid methods have been shown to be efficient and robust for iteration sequences with many dependent variables (such as arise in discretized PDEs) under a wide range of circumstances [3]. In this paper we report on the design and development of the first multigrid solvers for the particular set of Balance Equations which approximates the well-known Shallow-Water Equations in a rotating frame. The latter model is chosen, for simplicity, as a geophysically relevant analogue in two spatial dimensions of the 3D Primitive Equations. We demonstrate the effectiveness of the solvers with two types of initial-value problems in a periodic spatial domain: propagating dipolar vortices (called modons) and cascading turbulence with small viscosity. In both cases we explore, for both its mathematical and physical interest, the solution variations with R and F, and hence the Burger number B. We look at solutions over a

* Supported by the National Science Foundation through the National Center for Atmospheric Research, and by the United States–Israel Bilateral Science Foundation.

† Current address: The Department of Computer Science, Technion—Israel Institute of Technology, Haifa, Israel.

0021-9991/95 $6.00

range of Burger numbers, ranging from ones with the dominant motions on a scale comparable to the deformation radius to others where it is very much smaller (two-dimensional flow), in order to span the relevant geophysical regimes for large-scale motions in the ocean and atmosphere. A study of the limits of validity for balanced dynamics, which employs the present implicit solver along with a companion solver for the full Shallow-Water Equations, appears in [30]. There, we also study more extensively the matter of growth in time of perturbation (predictability).

2. SHALLOW-WATER BALANCE EQUATIONS

The basis for a general nondimensionalization when either R or F (defined below) is a small parameter is given in [24]. The resulting Shallow-Water Equations (SWE) are

$$R\frac{Du}{Dt} - v + [1, R]\phi_x = R\nu\mathcal{D}u, \tag{1}$$

$$R\frac{Dv}{Dt} + u + [1, R]\phi_y = R\nu\mathcal{D}v, \tag{2}$$

$$\mathrm{R}\frac{D\phi}{Dt} + \left(\frac{B}{[1, R]} + \mathrm{R}\phi\right)(u_x + v_y) = 0, \tag{3}$$

where the notation $[\cdot, \cdot]$ denotes the maximum of the arguments. Here u and v are the zonal and meridional velocities, respectively, and ϕ, the geopotential, is the nondimensional difference between the local absolute water-height, $\mathcal{H}^*$, and the mean height H^*, defined by

$$\phi = \frac{B}{R[1, R]}(\mathcal{H}^*/H^* - 1),$$

with the * superscript denoting dimensional quantities.

The nondimensional parameters used here and below are ν, the nondimensional viscosity coefficient, and

$$R = \frac{V^*}{f^*L^*}, \qquad F = \frac{V^*}{\sqrt{g^*H^*}}, \qquad B = \left(\frac{R}{F}\right)^2, \tag{4}$$

R being the Rossby number, F the Froude number, and B the Burger number. Here V^* is a characteristic velocity, g^* is the gravitational acceleration, f^* is the Coriolis frequency for the rotating environment, and L^* is a characteristic horizontal scale. The advection operator (material derivative) is defined by

$$\frac{D}{Dt} = \partial_t + u\partial_x + v\partial_y, \tag{5}$$

and $\mathcal{D}$ denotes some diffusion operator (e.g., the Laplacian, Δ, or the (negative) biharmonic operator, $-\Delta^2$; in all the numerical calculations reported here with $\nu \neq 0$ the biharmonic form of diffusion was used.)

In order to obtain the Shallow-Water Balance Equations (SWBE), we first take the curl and divergence of (1–2) and rewrite the resulting equations in the ζ (vorticity), ψ (stream-function) and χ (velocity potential) variables, defined up to additive constants for ψ and χ by

$$u = -\psi_y + \varepsilon\chi_x, \qquad v = \psi_x + \varepsilon\chi_y, \qquad \zeta = v_x - u_y, \tag{6}$$

where

$$\varepsilon = R\frac{[1, R]}{[1, B]}. \tag{7}$$

Note that $\varepsilon \ll 1$ when either $R \ll 1$ or $F \ll 1$. The resulting form of the SWE is

$$\frac{D\zeta}{Dt} + \left(\frac{[1, R]}{[1, B]} + \varepsilon\zeta\right)\Delta\chi = \nu\mathcal{D}\zeta, \tag{8}$$

$$\frac{D\phi}{Dt} + \left(\frac{B}{[1, B]} + \varepsilon\phi\right)\Delta\chi = 0, \tag{9}$$

$$\zeta - [1, R]\Delta\phi + 2RJ(\psi_x, \psi_y) - \varepsilon R\left\{\frac{D(\Delta\chi)}{Dt} + \mathcal{F}(\psi, \chi)\right\} = 0, \tag{10}$$

$$\zeta - \Delta\psi = 0, \tag{11}$$

where J is the Jacobian and $\mathcal{F}(\psi, \chi)$ is given by

$$\mathcal{F}(\psi, \chi) = 2[\psi_{xy}(\chi_{yy} - \chi_{xx}) + \chi_{xy}(\psi_{xx} - \psi_{yy})] + \varepsilon(\chi_{xx}^2 + \chi_{yy}^2 + 2\chi_{xy}^2).$$

The SWBE are obtained from (8–11) by dropping the $O(\varepsilon\mathrm{R})$ terms in (10), leaving

$$\zeta - [1, R]\,\Delta\phi + 2RJ(\psi_\psi, \psi_y) = 0. \tag{12}$$

The governing assumption in the derivation of the SWBE is $\varepsilon\mathrm{R} \ll 1$. This condition is satisfied when

$$R \ll 1 \qquad \text{and} \qquad B = O(1), F = O(R),$$

or when

$$B, R > 1 \qquad \text{and} \qquad F \ll 1.$$

This justifies a posteriori the choice of notation, which yields proper scaling in either of these extreme cases, the Quasigeo-

strophic limit ($R, F \to 0$) and the two-dimensional incompressible Navier Stokes limit ($F \to 0$, $B \to \infty$.)

2.1. *Initial Conditions*

Unlike the SWE, which are third-order in time, the SWBE (8–9, 11–12) form a system that is only first-order in time, and therefore requires a single initial condition over the entire domain of solution. A natural choice is to prescribe the vorticity at the initial time, $\zeta(x, y, 0)$. The streamfunction ψ can then be calculated from (11), and then the geopotential ϕ from (12), by solving the corresponding Poisson problems. Alternatively, we could have started with ψ, ϕ, or any other spatial differential functional of them, such as the potential vorticity, $\mathcal{P}$, defined in section 2.3 below. Calculation of the initial χ is less straightforward, and we now show that it requires the solution of a system of equations that is elliptic in the relevant regime of physical parameters. We first define two more variables, Φ and Ψ, to be the time-derivatives of ϕ and ψ respectively:

$$\Phi = \phi_t, \qquad \Psi = \psi_t. \tag{13}$$

Now, given ζ, ϕ and ψ as known functions at $t = 0$, and noting that, by (5) and (6), the material derivative can be written as

$$\frac{D}{Dt} = \partial_t + J(\psi, \cdot) + \varepsilon \nabla\chi \cdot \nabla, \tag{14}$$

the following linear system for χ, Φ, and Ψ is obtained from (8)–(11) and the time-derivative of (12).

$$\left(\frac{B}{[1, B]} + \varepsilon\phi\right)\Delta\chi + \varepsilon\nabla\chi\cdot\nabla\phi + \Phi = -J(\psi, \phi), \tag{15}$$

$$-[1, R]\Delta\Phi + \Delta\Psi + 2R[J(\psi_x, \Psi_y) - J(\psi_y, \Psi_x)] = 0, \tag{16}$$

$$\left(\frac{[1, R]}{[1, B]} + \varepsilon\zeta\right)\Delta\chi + \varepsilon\nabla\chi\cdot\nabla\zeta + \Delta\Psi = -J(\psi, \zeta) + \nu\mathcal{D}\zeta. \tag{17}$$

Let $\mathcal{A} = R^{-1} + \zeta$ and $\mathcal{H} = 1 + R[1, R]\phi/B$ denote the absolute vorticity and total height respectively. Then (15–17) can be written in matrix operator form as

$$\begin{pmatrix} L_{\mathcal{H}} & 1 & 0 \\ 0 & -[1, R]\Delta & M \\ L_{\mathcal{A}} & 0 & \Delta \end{pmatrix}\begin{pmatrix} \chi \\ \Phi \\ \Psi \end{pmatrix} = \begin{pmatrix} -J(\psi, \phi) \\ 0 \\ -J(\psi, \zeta) + \nu\mathcal{D}\zeta \end{pmatrix}, \tag{18}$$

where

$$L_{\mathcal{H}} = \frac{B}{[1, B]}\mathcal{H}\Delta + \varepsilon\nabla\phi\cdot\nabla = \frac{B}{[1, B]}\Delta + \varepsilon\nabla\cdot(\phi\nabla), \tag{19}$$

$$L_{\mathcal{A}} = \varepsilon(\mathcal{A}\Delta + \nabla\zeta\cdot\nabla) = \frac{\varepsilon}{R}\Delta + \varepsilon\nabla\cdot(\zeta\nabla), \tag{20}$$

and

$$\begin{aligned} M &= \Delta + 2R[J(\psi_x, \partial_y) - J(\psi_y, \partial_x)] \\ &= (1 + 2R\psi_{yy})\partial_{xx} + (1 + 2R\psi_{xx})\partial_{yy} - 4R\psi_{xy}\partial_{xy}. \end{aligned} \tag{21}$$

The operator at the left-hand side of (18) is elliptic so long as the total height $\mathcal{H}$ is positive everywhere (since the principal part of the operator, i.e., the highest-derivative term in the determinant (22), is positive definite: see below and also, e.g., the definition of ellipticity for systems in [10]).

2.2. *Preliminary Analysis*

An important first step in the construction of the numerical solver is to examine the differential system, in order to obtain some insight into its type and expected behavior, as well as its dependence on the various parameters.

We examine (18), arguing that if this problem is well-posed then the system can be integrated by the two-step algorithm of advancing ψ in time and then solving (11, 12, and 18) for the other variables at the new time-step. The determinant of the operator in (18) is

$$\mathrm{Det}_{18} = -([1, R]L_{\mathcal{H}}\Delta^2 - L_{\mathcal{A}}M). \tag{22}$$

It is straightforward to verify that

$$\mathcal{H} > 0 \Rightarrow -L_{\mathcal{H}} \text{ is elliptic positive definite,} \tag{23}$$

$$\mathcal{A} > 0 \Rightarrow -L_{\mathcal{A}} \text{ is elliptic positive definite,} \tag{24}$$

$$1 + 2R[\Delta\psi + 2RJ(\psi_x, \psi_y)] > 0 \Rightarrow -M \text{ is elliptic positive definite,} \tag{25}$$

where, by (12), the last condition can also be written as

$$1 + 2R[1, R]\,\Delta\phi > 0. \tag{26}$$

Note that each of these operators is self-adjoint. Also, (25) is the condition that the Dirichlet problem for the Monge-Amperè type equation (12), when solved for ψ with prescribed ϕ, have a unique solution. This follows from the proof of Rellich's theorem in [8, p. 324].

As noted above, Det_{18}, and therefore the operator at the left hand side of (18), is elliptic so long as the absolute height $\mathcal{H}$ is positive everywhere. However, since the coefficients of the operator vary in space, definiteness of the scalar operators in isolation does not necessarily imply well-posedness of the boundary-value problem associated with (18) (as it would in the constant-coefficient case for simple enough domains). This

question is probably best considered from the following point of view.

For simplicity we restrict ourselves to a 2π-doubly periodic domain. We only consider solutions whose spatial average vanishes, since ψ and χ can only be unique up to an additive constant, whereas for ζ this is an existence requirement (see below). The spatial average of ϕ vanishes by definition. In examining the issue of uniqueness it suffices to consider the homogeneous problem associated with (18), since if there are two solutions to (18) then their differences must satisfy the homogeneous system. Setting the right hand side of (18) to zero we obtain the following equation for χ

$$\chi - L_\chi \chi = 0, \tag{27}$$

where

$$L_\chi = [1, R]^{-1} L_{\mathcal{H}}^{-1} \Delta^{-1} M \Delta^{-1} L_{\mathcal{A}}. \tag{28}$$

(Similar equations can be obtained for Ψ and Φ). System (18) has a unique solution if and only if the trivial solution $\chi = 0$ to (27) is unique. Again, in the constant coefficient case uniqueness is very easy to show when conditions (23–25) hold, since all the operators involved have the same eigenfunctions, viz., Fourier functions, but it is as yet unsettled for the actual problem.

However, some insight into this matter can be obtained by applying $L_{\mathcal{H}}$ to (27), producing after rearrangement

$$\begin{aligned}[1, R]\left\{\frac{B}{[1, B]}\Delta + \varepsilon\nabla\cdot(\phi\nabla)\right\}\chi - \frac{\varepsilon}{R}\chi \\ = \varepsilon\Delta^{-1}[2\mathcal{J} + \nabla\cdot(\zeta\nabla) + 2R\mathcal{J}\Delta^{-1}\nabla\cdot(\zeta\nabla)]\chi,\end{aligned} \tag{29}$$

where

$$\mathcal{J} = J(\psi_x, \partial_y) - J(\psi_y, \partial_x).$$

Let $\langle a, b\rangle$ denote the inner product of a and b, defined by

$$\langle a, b\rangle = \int_D ab^*,$$

where D is our domain of solution. The inner product of (29) with χ yields after integration by parts

$$\begin{aligned}-\frac{[1, R]}{[1, B]} B\langle\mathcal{H}\nabla\chi, \nabla\chi\rangle - \frac{\varepsilon}{R}\langle\chi, \chi\rangle \\ = \varepsilon\langle\Delta^{-1}[2\mathcal{J} + \nabla\cdot(\zeta\nabla) + 2R\mathcal{J}\Delta^{-1}\nabla\cdot(\zeta\nabla)]\chi, \chi\rangle.\end{aligned} \tag{30}$$

χ is the solution to an elliptic problem. Hence, its first and second derivatives can be estimated (for sufficiently smooth ζ, which also implies by (12) sufficiently smooth ϕ), following, e.g., [10]. These bounds, (30) and the positivity of $\mathcal{H}$ can be employed to show uniqueness of solution for sufficiently small ε.

In summary, integration of the SWBE system is seen to require the inversion of an elliptic operator, as do its two limiting cases—the Quasigeostrophic equations and the two-dimensional incompressible Navier Stokes equations. But unlike these limits, the elliptic operator associated with the SWBE might be indefinite in certain regimes of parameters. The actual limits of solvability and accuracy are investigated in [30]. These limits need to be determined by numerical experimentation, since, even if the regime of parameters is such that the problem may be formally indefinite, the scale of components for which the operator changes sign may be far larger than the actual physical scales that appear. The ultimate test for the solution to the SWBE is the degree to which it approximates the solution to the SWE, and this property need not necessarily be closely related to formal properties of the elliptic operator.

2.3. *Integral Invariants*

The solution to the inviscid SWBE on a doubly periodic domain satisfies several integral invariants. Monitoring these is useful in gauging the performance of the solver.

Equations (8) and (9) can be written in the following form in terms of the variables $\mathcal{A}$ and $\mathcal{H}$

$$\frac{D\mathcal{A}}{Dt} + \varepsilon\mathcal{A}\Delta\chi = \nu\mathcal{D}A, \tag{31}$$

and

$$\frac{D\mathcal{H}}{Dt} + \varepsilon\mathcal{H}\Delta\chi = 0, \tag{32}$$

respectively, yielding

$$\frac{D\mathcal{P}}{Dt} = \mathcal{H}^{-1}\nu\mathcal{D}A, \tag{33}$$

where $\mathcal{P} = \mathcal{A}/\mathcal{H}$ is the potential vorticity. In the inviscid case $\nu = 0$, this yields the following integral invariants for the periodic domain.

$$\langle\mathcal{H}P^\eta\rangle = \text{constant} \tag{34}$$

for any η and all time. Here $\langle\cdot\rangle$ denotes the spatial average over the domain of solution, which is assumed to be finite initially. In particular, letting $\eta = 0$ and $\eta = 1$, respectively, yields

$$\langle\phi\rangle, \langle\zeta\rangle = \text{constant}. \tag{35}$$

By (11) $\langle\zeta\rangle$ must actually be zero for all time for a solution to

exist. The constant $\langle\phi\rangle$ is zero by definition, since we chose ϕ to denote the difference between the local height and the mean height. Equation (34) with $\eta = 2$ implies conservation of the spatially averaged *potential enstrophy* $\mathcal{H}P^2$. The SWBE do not conserve energy (see the discussion in [13].)

3. NUMERICAL SOLVERS

Ever since their introduction systems of Balance Equations have been considered difficult to solve. The reason for this difficulty is seen in Section 2.2 to be that the initialization, and therefore also any explicit solution process, requires inverting an elliptic matrix operator with non-constant coefficients. In [20] the first effective solution to such a system was presented. The approach employed was (in effect) to iterate at each time-level by inverting the constant-coefficient part of the elliptic operator (which, being a product of Laplace and Helmholtz operators could be efficiently inverted by direct methods on simple enough domains), while freezing the non-constant part for the duration of the iteration. As can be expected, this approach is efficient whenever ε is small, since the non-constant part is then relatively small, but must become less efficient and eventually fail as ε becomes larger. This can be seen by the following general analysis.

Consider the system

$$Lu = (L_c + \varepsilon L_v)u = f,$$

Where L is some linear operator, L_c is an easily invertible constant-coefficient operator, L_v is a variable-coefficient operator that is difficult to invert, and ε is a parameter. (In the SWBE the leading order term in L_v does not depend on ε. Higher-order terms do, but this dependence is unimportant in the present analysis.)

Consider the iteration procedure,

$$u^n = -L_c^{-1}(f - \varepsilon L_v u^{n-1}),$$

where the superscripts denote the iteration number. Let e^n and e^{n-1}, denote the error, i.e., the difference between the exact solution u and the approximate solutions at iteration n and $n - 1$, respectively. The errors satisfy

$$e^n = -\varepsilon L_c^{-1} L_v e^{n-1}.$$

Hence, the *asymptotic* rate of convergence of this iteration scheme is determined by product of ε and the *spectral radius*, i.e., the largest (in absolute value) eigenvalue of $L_c^{-1}L_v$. Clearly, this iteration process may be efficient when ε is small, but loses this efficiency when ε is larger and eventually fails. The limits of solvability with this approach can be extended somewhat by employing various methods of under-relaxation or continuation (embedding), but the cost of solution then increases rapidly.

A qualitative assessment of the number of iterations per time-step that are required with this approach can be obtained by arguing that in order to maintain qth-order spatial accuracy (using an appropriate discretization) the *algebraic error* (i.e., the difference between the solution to the discrete equations and the approximate solution obtained by the iteration process) needs to be reduced well below the spatial truncation error of the increment in the solution from each time-level to the next, which is proportional to h^q. This must hold for all the scales that are approximable on the finest grid (see [5, sect. 2.3] and also [3, sect. 7].) Hence, if ρ denotes the aforementioned spectral radius, then n_i, the number of iterations required per time-level is approximately

$$n_i \geq q \frac{\log(ch)}{\log(\varepsilon\rho)},$$

for some c independent of h, with ch and $\varepsilon\rho$ smaller than one. Note that this is an asymptotic assessment. A small number of iterations may exhibit different behavior. Indeed, there may conceivably be an increase in the error for several iterations even if $\varepsilon\rho$ is smaller than one.

As $\varepsilon\rho$ approaches one the required number of iterations may become quite large. But multigrid techniques are able to overcome this limitation to a great extent. The multigrid approach described in this section can also be viewed as an iteration process in which part of the operator is frozen on each level. But, by taking care to include the principal part of the operator on all the levels (that is, the dominant terms on the scale treated at each level), we are assured, by definition, that the frozen part is relatively small. Recognition of the principal part on each level is obtained by the *coupling analysis* (see below and Appendix).

3.1. *Temporal Discretization*

Two approaches for constructing multigrid solvers to the SWBE, discretized by finite differences, are proposed, one based on explicit time-stepping, and one on implicit treatment of the time-derivatives.

A natural explicit time-stepping algorithm is suggested by the method of calculating initial conditions described in Section 1.1 above. Given the solution at time-levels 0, ..., $n - 1$, the solution at time-level n is calculated as follows, with superscripts denoting the time-level.

1. Calculate ψ^n by some explicit time-stepping method from Ψ and ψ at time-levels 0, ..., $n - 1$.
2. Calculate ζ^n by (11).
3. Solve (12) for ϕ^n.
4. Solve (18) at time-level n for χ^n, Φ^n, and Ψ^n.
5. If using a predictor-corrector type method (see Section 3.2) perform a correction step by repeating Steps 1–4, while employing Ψ^n calculated in Step 4 of the predictor to obtain an improved estimate for ψ^n in Step 1 of the corrector.

Solution to (11, 12, and 18) is obtained by the multigrid algorithm described in Section 3.3 below.

Fully implicit solution of (8–9, 11–12) requires temporal discretization of the first terms in (8) and (9). We employ Crank–Nicholson discretization and obtain the following system. (Note that we only write this system in matrix form for convenience, and no linearization is implied.)

$$\begin{pmatrix} \frac{1}{\Delta t}+\frac{1}{2}(\mathbf{v}\cdot\nabla-\nu\mathcal{D}) & 0 & \frac{1}{2}\varepsilon\mathcal{A}\Delta & 0 \\ 0 & \frac{1}{\Delta t}+\frac{1}{2}\mathbf{v}\cdot\nabla & \frac{1}{2}\frac{B}{[1,B]}\mathcal{H}\Delta & 0 \\ 1 & -[1,R]\Delta & 0 & 2RJ(\partial_x,\partial_y) \\ 1 & 0 & 0 & -\Delta \end{pmatrix}^{n} \begin{pmatrix} \zeta \\ \phi \\ \chi \\ \psi \end{pmatrix}^{n}$$

$$= \begin{pmatrix} \frac{1}{\Delta t}-\frac{1}{2}(\mathbf{v}\cdot\nabla-\nu\mathcal{D}) & 0 & -\frac{1}{2}\varepsilon\mathcal{A}\Delta & 0 \\ 0 & \frac{1}{\Delta t}-\frac{1}{2}\mathbf{v}\cdot\nabla & -\frac{1}{2}\frac{B}{[1,B]}\mathcal{H}\Delta & 0 \\ 0 & 0 & 0 & 0 \\ 0 & 0 & 0 & 0 \end{pmatrix}^{n-1} \begin{pmatrix} \zeta \\ \phi \\ \chi \\ \psi \end{pmatrix}^{n-1}, \tag{36}$$

where $\mathbf{v}\cdot\nabla = J(\psi, \cdot) + \varepsilon\nabla\chi\cdot\nabla$ is the spatial advection operator, Δt is the time-step, and the superscripts denote the time-level. The equations are thus staggered in time, the first two centered at the midpoint between time-levels, and the third and fourth at the new time-level. The details of the multigrid algorithm for (36) are also described in Section 3.3.

Crank–Nicholson discretization for the advection operator with purely imaginary eigenvalues of the spatial operator (such as the central differencing we employ) has only marginal linear stability (see, e.g., [14 or 23]). Over a long integration the nonlinear interactions can lead to computational instabilities. This problem can be solved simply by various methods, such as are frequently used with the explicit Leapfrog scheme. We used simple averaging of two consecutive solutions every two hundred time steps, which eliminated this instability with very little effect on the accuracy.

Note that the algorithms we use can be applied with any temporal discretization that is suitable for advection problems, both in the explicit and implicit time formulations, and our particular choices are not a necessary part of the approach.

3.2. *Explicit Time-Stepping Procedure*

In our calculations we use the predictor-corrector type Leapfrog-Trapezoidal (LT) scheme [15], defined as follows. Consider the equation

$$u_t = Lu. \tag{37}$$

Given the solution u at time-levels n and $n-1$, the LT scheme for calculating the solution at time-level $n+1$ is defined as follows.

$$u^p = u^{n-1} + 2\Delta t L u^n \tag{38}$$

$$u^{n+1} = u^n + 0.5\Delta t(Lu^n + Lu^p), \tag{39}$$

where the superscripts denote time-levels, p denoting the predicted value. By Von Neuman stability analysis for the constant-coefficient advection equation, it is easy to verify that LT is stable up to Courant number $\sqrt{2}$ in the inviscid case, and remains stable with the addition of $O(h)$ (Laplacian) viscosity for slightly smaller Courant numbers. Furthermore, LT has no spurious numerical modes such as appear in Leapfrog. The LT scheme is also slightly more accurate than Leapfrog, inasmuch as the leading-order temporal truncated term is half as large, but it is about twice as costly per time-step. Hyman (in [14 and references therein]) suggests various alternatives for the corrector used with the Leapfrog predictor, that yield higher-order schemes with still better linear stability properties at comparable effort.

3.3. *Spatial Discretization*

The choice of spatial discretization involves considerations such as accuracy, computational cost, multigrid smoothing properties of the associated relaxation schemes (Sections 3.3 and 3.4 below), conservation properties and integral invariants. The last two are best handled by writing out and discretizing

the equations in flux form. Here we chose to write $J(\psi, \cdot)$, $J(\psi_x, \psi_y)$, $J(\psi_x, \partial_y)$ and $J(\psi_y, \partial_x)$ respectively as

$$J(\psi, \cdot) = (\psi_x \cdot)_y - (\psi_y \cdot)_x,$$

$$J(\psi_x, \psi_y) = \frac{1}{2}\left[\nabla \cdot (\Delta\psi \nabla\psi) - \frac{1}{2}\Delta(\nabla\psi \cdot \nabla\psi)\right],$$

$$J(\psi_x, \partial_y) = (\psi_{xx}\partial_y)_y - (\psi_{xy}\partial_y)_x,$$

$$J(\psi_y, \partial_x) = (\psi_{yx}\partial_x)_y - (\psi_{yy}\partial_x)_x.$$

The spatial discretization we employ is a straightforward second-order central differencing of the terms in flux form. Laplacians are discretized by the usual five-point discretization, denoted Δ^h below. The other terms are discretized as indicated below, with h superscripts denoting discrete approximations. Subscripts denote the mesh-point at which the term is discretized, with, e.g., subscript $i + 1/2, j$ denoting the average of the values at nodes $i + 1, j$ and $i, j \cdot h$ is the mesh-size.

$$J^h(\psi, \zeta) = \frac{1}{4h^2}\{[\zeta_{i,j+1}(\psi_{i+1,j+1} - \psi_{i-1,j+1}) - [\zeta_{i,j-1}(\psi_{i+1,j-1} - \psi_{i-1,j-1})] - \zeta_{i+1,j}(\psi_{i+1,j+1} - \psi_{i+1,j-1}) - \zeta_{i-1,j}(\psi_{i-1,j+1} - \psi_{i-1,j-1})]\},$$

with $J^h(\psi, \phi)$ defined similarly.

$$\nabla^h \cdot (\zeta\nabla^h\chi) = \frac{1}{h^2}[\zeta_{i+1/2,j}\chi_{i+1,j} + \zeta_{i-1/2,j}\chi_{i-1,j} + \zeta_{i,j+1/2}\chi_{i,j+1} + \zeta_{i,j-1/2}\chi_{i,j-1} - (\zeta_{i+1/2,j} + \zeta_{i-1/2,j} + \zeta_{i,j+1/2} + \zeta_{i,j-1/2})\chi_{i,j}],$$

with $\nabla^h \cdot (\zeta\nabla^h\phi)$ and $\nabla^h \cdot (\zeta\nabla^h\psi)$ defined similarly.

$$\Delta^h(\nabla^h\psi \cdot \nabla^h\psi) = \Delta^h[(\partial_x^h\psi)^2 + (\partial_y^h\psi)^2],$$

where

$$\partial_x^h\psi = \frac{1}{2h}[\psi_{i+1,j} - \psi_{i-1,j}],$$

$$\partial_y^h\psi = \frac{1}{2h}[\psi_{i,j+1} - \psi_{i,j-1}].$$

$$(\psi_{xx}\Psi_y)_y^h = \frac{1}{4h^4}[(\psi_{i+1,j+1} - 2\psi_{i,j+1} + \psi_{i-1,j+1})(\Psi_{i,j+2} - \Psi_{i,j}) - (\psi_{i+1,j-1} - 2\psi_{i,j-1} + \psi_{i-1,j-1})(\psi_{i,j} - \Psi_{i,j-2})],$$

$$(\psi_{yy}\Psi_x)_x^h = \frac{1}{4h^4}[(\psi_{i+1,j+1} - 2\psi_{i+1,j} + \psi_{i+1,j-1})(\Psi_{i+2,j} - \psi_{i,j}) - (\psi_{i-1,j+1} - 2\psi_{i-1,j} + \psi_{i-1,j-1})(\Psi_{i,j} - \Psi_{i-2,j})],$$

$$(\psi_{xy}\Psi_y)_x^h = \frac{1}{16h^4}[(\psi_{i+2,j+1} + \psi_{i,j-1} - \psi_{i+2,j-1} - \psi_{i,j+1})(\Psi_{i+1,j+1} - \Psi_{i+1,j-1}) - (\psi_{i,j+1} + \psi_{i-2,j-1} - \psi_{i,j-1} - \psi_{i-2,j+1})(\Psi_{i-1,j+1} - \Psi_{i-1,j-1})],$$

$$(\psi_{yx}\Psi_x)_y^h = \frac{1}{16h^4}[(\psi_{i+1,j+2} + \psi_{i-1,j} - \psi_{i-1,j+2} - \psi_{i+1,j})(\Psi_{i+1,j+1} - \Psi_{i-1,j+1}) - (\psi_{i+1,j} + \psi_{i-1,j-2} - \psi_{i-1,j} - \psi_{i+1,j-2})(\Psi_{i+1,j-1} - \Psi_{i-1,j-1})].$$

With this discretization the consistency condition for existence of solution is the same as for the differential system, (35), with the integrals replaced by sums.

3.4. *Multigrid Algorithm*

The basic element of the multigrid solver is the correction cycle [2, 3]. We first describe in detail the bigrid (two-level) correction cycle, employing the Full Approximation Scheme (FAS) [3, sect. 8], and then define the multigrid cycle. FAS is necessary in the implicit approach due to the nonlinearity, and we recommend it in the explicit approach as well, as it is necessary for further developments of the solver (e.g., for local refinement). We use here the notation of [3, sect. 8].

3.4.1. *Bigrid Correction Cycle.* Consider the discretized problem

$$L^h u^h = f^h. \tag{40}$$

Starting with some approximation to u^h, a bigrid (or two-level) correction cycle is employed to reduce the error in the approximation. This cycle has two main phases, the relaxation, or error-smoothing, phase and the coarse-grid correction. In the error-smoothing phase several *relaxation sweeps* are performed by scanning all the variables defined on grid h, and applying some (usually local) relaxation iteration (e.g., Gauss–Seidel, SOR, or Jacoby) to (40), whose purpose is to smooth the error by greatly reducing the amplitude of such small-scale (high-wavenumber) error components that are defined on the fine grid h, but alias with larger-scale components on a coarser grid H. In the coarse-grid correction phase the problem is transferred to the coarse grid, where the remaining error-components (i.e., those that are also defined on grid H) are reduced.

The bigrid cycle is performed as follows. Equation (40) is relaxed ν_1 times, where ν_1 is some small integer (see also Section 3.4 below), producing an approximate solution $\tilde{u}^h$, whose corresponding error v^h, defined by

$$v^h = u^h - \tilde{u}^h,$$

is smooth on the scale of the grid. Therefore, (40) can be approximated on a coarser grid H, whose mesh-size is normally chosen to be $H = 2h$. The coarse-grid problem is

$$L^H \hat{u}^H = \hat{f}^H, \tag{41}$$

where

$$\hat{f}^H = L^H(\hat{I}_h^H \tilde{u}^h) + I_h^H r^h. \tag{42}$$

Here, L^H is the coarse-grid approximation to L^h, $\hat{u}^H$ is the coarse-grid variable, and $\hat{I}_h^H$ and I_h^H are some fine-to-coarse transfer (restriction) operators, which need not be the same. r^h, the fine-grid residual, is given by

$$r^h = f^h - L^h \tilde{u}^h. \tag{43}$$

Having obtained a sufficiently good approximation, $\tilde{u}^H$, to $\hat{u}^H$ in (41), the approximate coarse-grid correction $\tilde{v}^H$, defined by

$$\tilde{v}^H = \tilde{u}^H - \hat{I}_h^H \tilde{u}^h, \tag{44}$$

is interpolated and added to the fine-grid approximation

$$\tilde{u}_{new}^h = \tilde{u}^h + I_H^h \tilde{v}^H, \tag{45}$$

where I_H^h is a coarse-to-fine (interpolation) operator. Finally, (40) is relaxed ν_2 (small integer) times. There are called post-relaxation sweeps, while the sweeps that precede coarse-grid correction are called pre-relaxation sweeps.

3.4.2. *Multigrid Correction Cycle.* In the two-level algorithm defined above the manner in which the approximate solution to the coarse-grid problem (41) is obtained is not prescribed. This is usually done recursively, by now considering grid H as the fine grid and applying γ (small integer) similar correction cycles, employing a still coarser grid for correcting the error components that are smooth on scale H. The resulting coarse-grid problem can employ a still coarser grid within yet more correction cycles and so on, until such a coarse grid is reached that solution by repeated relaxation sweeps or direct methods is negligible.

Usually, it suffices to prescribe γ, the *cycle-index*, to be one (yielding the so-called V cycle), or two (yielding a W cycle) [3, sect. 1]. In the present problem the simple V cycle, with one pre-relaxation sweep and one post-relaxation sweep, is normally sufficient, but, as will be seen below, more relaxation sweeps may be necessary on the coarsest grids in "difficult" regimes of physical parameters, due to reduced smoothing efficiency. The extra cost involved is negligible except in extreme cases.

3.4.3. *F Cycle.* The multigrid solution of the time-dependent problem defined by the discretized SWBE is essentially reduced to the solution of a boundary-value problem for the increment in the solution at each time-level (that is, the difference between the solutions at consecutive time-levels). This is done by employing an F cycle [5], defined below, which is in effect a Full Multigrid (FMG) algorithm [3] for the increment in the solution. In particular, this cycle has the important property that, if the solution is already at steady state, it will remain unchanged with each additional time-level, since the increment in the solution is zero.

The F cycle is defined by the following algorithm:

1. Beginning with an initial fine-grid approximation from the previous time-level, transfer residuals and approximate solution and construct the right-hand side of the second-finest grid problem, as in (42) and (43) in the FAS multigrid cycle. Repeat this process on the next-coarser grid and so on, until right-hand sides have been defined on all grids. No relaxation is performed during this stage.

2. Solve the problem on the coarsest grid, directly or by repeated relaxation. Interpolate and add the correction given by this solution to the second-coarsest grid approximation as in (45).

3. Repeat step 2 on the second-coarsest grid, employing δ (small integer) FAS multigrid correction cycles for the solution to the problem on the second-coarsest grid. Repeat this process on the next-finer grid and so on, until the finest grid, ending with δ' cycles on the finest grid.

In the present application, as usual, $\delta = \delta' = 1$ (denoted 1-F

cycle) apparently suffices to reduce the algebraic error well below the level of truncation errors of the increment.

3.5. *Relaxation and Intergrid Transfers*

The most important phase in developing multigrid solvers is the construction of efficient smoothers (relaxation schemes). Frequently, point Gauss–Seidel is the simplest and most efficient form of relaxation. A Gauss–Seidel relaxation sweep for a single equation is performed by scanning all the variables in some prescribed order and changing each variable in turn so as to satisfy the equation which corresponds to this variable. More generally, this change can be reduced (amplified) by multiplying it by some positive factor S, that is smaller (greater) than one, yielding under-relaxation (over-relaxation). As noted in [28], under-relaxation may prove useful in certain extreme cases.

A coupling analysis, introduced in [28], is applied to the systems (in the Appendix), and it shows that *weakly coupled* configurations are obtainable for both systems, and therefore the equations in the systems can be relaxed (on fine enough grids) as if they were decoupled. (In the language of [3, sect. 3], this means that a one-to-one correspondence between variables and equations exists such that the principal parts of the linearized matrix operators are diagonal matrices). In (18) this entails relaxing the first equation for χ, the second for Φ and the third for Ψ. In the implicit approach, the first equation in (36) must be relaxed for ζ, the second for χ, the third for ϕ and the fourth equation for ψ. The coupling analysis then shows that (18) is weakly coupled, its *smoothing factor* (i.e., worst reduction factor per fine-grid relaxation sweep of error-components that are not approximable on a twice-coarser grid) being approximately equal to that of the Laplace operator, under the following condition

$$\left[\left|\frac{R}{B}\mathcal{P}[1,R]h^2\right|^{1/3}, \frac{\varepsilon[1,B]}{B\mathcal{H}}h\right] \ll 1, \tag{46}$$

where the second term represents the non-principal term in $L_{\mathcal{H}}$, $\varepsilon\nabla\phi\cdot\nabla$. It is assumed that the variables and their first derivatives are O(1).

Let $\alpha = \Delta t/h$ denote the ratio between the time-step and the mesh-size. Then the coupling analysis for (36) implies that the smoothing factor of the system is approximately equal to the worse (larger) of the smoothing factors of the Laplace operator and the advection-diffusion operator that operates on ζ in the first equation of (36), under the following condition:

$$\left[\alpha h^2, \left|\alpha\frac{R}{B}\mathcal{P}[1,R]h^2\right|^{1/2}, \left|\frac{R}{B}\mathcal{P}[1,R]h^2\right|^{1/3}, \frac{\varepsilon[1,B]}{B\mathcal{H}}h\right] \ll 1. \tag{47}$$

The first term in (47) equals $h\Delta t$, which is clearly small on all grids. The second term is dominated by the third term on all grids (unless the time-step is unrealistically large). Hence, it suffices to consider the last two terms in (47), which are the same as the terms in (46). The fourth term in (47) is small on all grids so long as the water height is not very small. But the third term in (47) is $O(h^2/B)^{1/3}$ when R is small or moderate, and $O(Fh)^{2/3}$ when R is moderate or large. While B (which is the square of the non-dimensional radius of deformation) must be large compared to the square of the finest mesh-size in order to resolve the energy-containing scales of the physical phenomena, this term may not be small on the coarsest grids. However, following [3, sect. 3.7], (19–22) suggest that efficient relaxation is obtainable whenever ε is small, since, when $\varepsilon \to 0$, Det_{18} reduces to a product of Laplace operators and a Helmholtz operator, each of which can be relaxed very efficiently on all grids. This efficiency can be obtained by an implicit transformation of variables in the form of distributive relaxation [3, 28], such that the system for the transformed variables will be weakly coupled whenever ε is sufficiently small. The simplest way to do this is by right-multiplying the matrix operator at the left hand side of (18) by a *distribution matrix*, D_{18}, such that the product tends to a triangular matrix when $\varepsilon \to 0$. We know that the diagonal elements of the product must tend to two Laplace operators and a Helmholtz operator when $\varepsilon \to 0$, suggesting the following for D_{18}.

$$D_{18} = \begin{pmatrix} 1 & 0 & 0 \\ -\varepsilon\mathcal{A}/[1,R] & 1 & 0 \\ -\varepsilon\mathcal{A} & 0 & 1 \end{pmatrix} \tag{48}$$

yielding the following product with (18):

$$\begin{pmatrix} L_{\mathcal{H}} - \varepsilon\mathcal{A}/[1,R] & 1 & 0 \\ (\Delta - M)\varepsilon\mathcal{A} & -[1,R]\Delta & M \\ L_{\mathcal{A}} - \varepsilon\Delta\mathcal{A} & 0 & \Delta \end{pmatrix}. \tag{49}$$

The matrix in (48) implies the following relaxation process: apply Gauss–Seidel relaxation to the third, then the second equation as usual; then relax the first equation by scanning the mesh-points in the prescribed order (see below) and introducing changes in all three variables at each location, that are proportional to the respective entries in the first column of D_{18}, such that the residual (of the corresponding χ-equation) will vanish. That is, in order to implement the distributive relaxation for the χ-equation at meshpoint (i, j), one adds an increment δ to $\chi_{i,j}$, but also adds $-\varepsilon\delta\mathcal{A}/[1, R]$ to $\Phi_{i,j}$ and $-\varepsilon\mathcal{A}\delta$ to $\psi_{i,j}$, choosing such a δ that the residual of the relaxed χ-equation will vanish.

The coupling analysis for (49) also appears in Appendix A. The condition for weak coupling is now

$$\left[\frac{R^2|\mathcal{P}|}{B}h^2, \left\{\frac{\varepsilon[1,B]}{B\mathcal{H}}h^3\right\}^{1/2}, \frac{\varepsilon[1,B]}{B\mathcal{H}}h\right] \ll 1. \tag{50}$$

Evidently, the transformed system is weakly coupled whenever ε is small compared to B regardless of the mesh-size, and also whenever the mesh-size is small, even if ε is not. Indeed, there is a quantitative decrease in the coupling on all scales in the potentially troublesome small to moderate B regime. This and the fact that the additional cost and complication involved in applying this distributive relaxation is very small suggest that the distributive relaxation should be used on all grids.

Finding the appropriate distribution matrix for the implicit solver, (36), is more difficult. Indeed, now two matrices are required, one which multiplies the matrix operator from the left, and one from the right. The former is equivalent to subtracting (9), multiplied by $[1, R]/B$, from (8), and using this equation instead of (8). The resulting system, linearized for the present analysis, can be written as

$$\begin{pmatrix} D_t & L_{\mathcal{A}} - [1,R]L_{\mathcal{H}}/B & -[1,R]D_t/B & -J(\zeta,\cdot) + [1,R]J(\phi,\cdot)/B \\ 0 & L_{\mathcal{H}} & D_t & -J(\phi,\cdot) \\ 0 & 0 & -[1,R]\Delta & M \\ -1 & 0 & 0 & \Delta \end{pmatrix} \begin{pmatrix} \zeta \\ \chi \\ \phi \\ \psi \end{pmatrix} = 0. \tag{51}$$

The distribution (right-multiplying) matrix for (51) is chosen to be

$$D_{51} = \begin{pmatrix} 1 & 0 & 0 & 1/B \\ 0 & 1 & 0 & 0 \\ 0 & 0 & 1 & 1/[1,R] \\ 0 & 0 & 0 & 1 \end{pmatrix}, \tag{52}$$

which yields the following product with (51):

$$\begin{pmatrix} D_t & L_{\mathcal{A}} - [1,R]L_{\mathcal{H}}/B & -[1,R]D_t/B & -J(\zeta,\cdot) + [1,R]J(\phi,\cdot)/B \\ 0 & L_{\mathcal{H}} & D_t & D_t/[1,R] - J(\phi,\cdot) \\ 0 & 0 & -[1,R]\Delta & M - \Delta \\ -1 & 0 & 0 & \Delta - 1/B \end{pmatrix}. \tag{53}$$

(52) implies that the first, then second, then third equation be relaxed for ζ, χ and ϕ as usual (see below), and then the fourth equation be relaxed by introducing changes in ψ, ϕ and ζ at each mesh-point, that are proportional to the corresponding entries in D_{48}, such that will make the residual of the fourth equation at that point vanish.

The coupling analysis for (53), which also appears in the Appendix, yields the following condition for weak coupling.

$$\left[\frac{B+[1,R]}{B+h^2}\alpha h^2, \frac{\varepsilon[1,B](B+[1,R])}{B\mathcal{H}(B+h^2)(\alpha+[1,R])}\alpha^2 h^2, \left\{\frac{R^2(B+[1,R])}{B\mathcal{H}(B+h^2)}h^2\right\}^{1/2}, \frac{\varepsilon[1,B]}{B\mathcal{H}}h\right] \ll 1. \tag{54}$$

The first term in (54) is $O(h\Delta t)$ when B is moderate. When B is small compared to h^2 the first term becomes $O(\alpha)$. But this can occur only on the coarse grids, where α is small. Hence, this term is small on all the levels. The other terms in (54) are easily seen to be small whenever either ε or h is small compared to B, unless the absolute water-height is very small. Once more there is a quantitative weakening of coupling on all the grids at relatively small cost, and the distributive relaxation is recommended on all levels.

Gauss–Seidel relaxation in Red–Black ordering of the Laplace operator is known to yield the excellent smoothing factor of 0.25 (with one or two relaxation sweeps per level; see, e.g., [26]). The advection operator's smoothing factor depends on such factors as α (more precisely the Courant number, defined in (55) below), the size of the viscosity coefficient compared to the mesh size, and the degree of alignment of the flow with the grid. Since Gauss–Seidel relaxation fails (with the present

discretization) for moderately large Courant numbers, a slightly more elaborate relaxation method is employed for relaxing ζ in the first equation of (51): Kaczmarz relaxation, whereby the variables are scanned (in Red–Black order), and the equation at each point is satisfied in turn by introducing changes in the ζ variables participating in the discretization at that point, that are proportional to the coefficients of the variables in the discretization stencil (see [27] for general formulation, and also [3, sect. 1]). Applying Kaczmarz relaxation to some matrix A is equivalent to applying Gauss–Seidel relaxation to AA^T. Hence, this is generally a very useful relaxation scheme for the advection–diffusion operator with small diffusion coefficient, since it is always stable (AA^T being symmetric positive definite).

For the interpolation operator I_H^h in (45) we employ bi-cubic interpolation, in the correction V cycles as well as in the F cycles. The residual-transfer operator I_h^H in (42) is the usual full-weighted transfer (the adjoint of bilinear interpolation). The solution is also transferred by this full-weighting operator ($\hat{I}_h^H$ in (42) and (44)), so as to maintain the same sum of the field over the domain on the coarse grid.

3.6. *Computational Cost*

The computational cost of multigrid solvers is customarily measured in *work units*. A work unit is defined as the cost of calculating the residuals on the finest grid for the entire system. Hence, its cost is proportional to the number of grid points and it depends on the number of equations and their complexity and on the discretization. Thus, calculation of residuals on the finest grid costs one work unit, as does point Gauss–Seidel relaxation. Kaczmarz relaxation and distributive Gauss-Seidel are somewhat more expensive. However, in the present application, Kaczmarz is only used in the implicit solver, and only for one of the four equations, and the distributive relaxation employed is extremely simple. Hence, the cost of relaxation is only increased by a small fraction.

If some operation is carried out similarly on all the grids (and in each cycle the number of visits to all the levels is the same, as in the V cycle and F cycle), and its cost on the finest grid is c, then the total cost is about $c[1 + (2^d - 1)^{-1}]$, where d is the number of spatial dimensions (since the work on each grid is 2^d times as great as the work on the next-coarser grid. This does not take into account the fact that, when vector or parallel computing is employed, the computation is relatively less efficient on the coarse grids. However, this effect is small so long as the finest three or four levels are treated with full efficiency). Hence, the total work (measured in work units) decreases at higher dimensions, since the work on the coarse grids is relatively smaller. We therefore expect greater efficiency in three-dimensional calculations than is exhibited in the two-dimensional case here.

With the exception of negligibly small extra work on the coarsest grids we use a $V(1,1)$ cycle (i.e., a multigrid cycle with cycle-index $\gamma = 1$, one pre-relaxation sweep and one post-relaxation sweep), within a 1-F cycle (i.e., an F cycle with one cycle per refinement). Hence the cost of relaxation is $2 \times \frac{4}{3} \times \frac{4}{3}$ work units, plus an additional small fraction due to the somewhat elaborate relaxation schemes. Residual calculations within the V cycles require $\frac{16}{9}$ work units per time-level. Use of FAS requires evaluating the operator for the right-hand sides on all grids but the finest for $\frac{4}{9}$ more work units. In addition, the initial residual-calculation and FAS of the F cycle requires $\frac{5}{3}$ work units. The rest of the cost is due to transfer operations (restriction of the solution and residuals and interpolation). These are very inexpensive compared to the cost of discretization in the present application. Hence, the total cost per time-level is about nine work units.

The explicit solver requires about twice as many work units as the implicit solver, since it is of predictor-corrector type, and the cost of its work unit is comparable to that of the implicit solver.

In comparison, existing solvers require about one work unit per iteration plus the cost of inverting the associated Laplacian and Helmholtz operators. Thus, for sufficiently small ε they are less expensive when just a few iterations suffice. However, the present solver can then be made still more efficient by similarly freezing the ε-dependent terms during the multigrid cycles, and also changing from FAS to CS (Correction Scheme) mode, thereby reducing the cost of solution significantly. This can be incorporated in the solvers, and is one of many ways of optimizing their efficiency. When ε is larger, however, the number of iterations required in the single-grid approach grows rapidly, while the extra work required in the multigrid solver increases very slowly, since only coarse-grid work is increased. Also, the implicit solver poses no CFL stability restriction on the time-step.

In summary, the total cost of integration over an interval of time T with the implicit solver is about $9T/\Delta t$ work units. The cost per time-level gradually increases when the Courant number, defined in (55), is increased above two or three, since smoothing efficiency of the advection operator decreases, and more relaxation sweeps of this operator are therefore required. However, the additional cost up to Courant number of about twelve was found to be less than 50%. A further assessment of the computational cost is made in Section 4 below.

4. NUMERICAL EXPERIMENTS

Numerical experiments confirming the error-reduction efficiency of the correction-cycles for (18) and (36) are reported in [28]. But the corresponding relaxation schemes fail, as predicted by the coupling analyses, when B is small compared to the square of the mesh-size, and the distributive schemes defined by (48) for the explicit formulation and by (52) for the implicit formulation must be employed. We tested the solvers with two types of initial-value problems in a 2π-periodic spatial domain: modons (propagating dipolar vortices [11]) and cascading turbulence with small viscosity. Calculations were carried

out with both solvers to examine asymptotic error-reduction efficiency, effects of variation of the Rossby number and Burger number, CFL stability constraints, effects of large time-steps (with the unconditionally stable implicit solver) on accuracy and efficiency, and various points of physical interest.

The important parameter with respect to linear stability and temporal accuracy is the Courant number C defined by

$$C = \frac{\Delta t}{h} \max(|\psi_{x+R_{\chi_y}}| + |\psi_y - R\chi_x|), \tag{55}$$

where the maximum is taken over the spatial domain of solution. Also, since the physical properties of the flow are, of course, determined by the main flow structures and not by the choice of domain size or precise scaling of variables, we define more meaningful, *locally* scaled non-dimensional parameters, R' and B', by

$$R' = R|\zeta_{\min}|, \tag{56}$$

and

$$B' = \frac{R'[1, R']}{1 - \mathcal{H}_{\min}} = \frac{B}{|\phi_{\min}|} \frac{R'[1, R']}{R[1, R]}, \tag{57}$$

where (r, θ) are cylindrical coordinates in the translating reference frame, J_i and K_i are Bessel functions of order i,

$$p^2 = A^2/B, \tag{59}$$

and k is the first (i.e., smallest) wavenumber to satisfy

$$K_2(p)/pK_1(p) + J_2(k)/kJ_1(k) = 0. \tag{60}$$

In our numerical calculations we choose $A = 0.3\pi$, which is sufficiently small to make the "boundary" effects due to the spatial periodicity negligible, yet sufficiently large to be well resolved by the 256^2 uniform grid on which the problem was discretized. All the calculations are performed with $B = 1/16$, yielding $B' \approx 1$. Since seven levels are used in the solvers, the coarsest grid being 4^2, B is of the order of the square of the mesh-size of the intermediate grids and quite small compared to the coarsest mesh-sizes employed. These parameters yield $k = 4.303205$ as the first solution to (60). We then chose c, the propagation velocity, to be 0.1, in order to obtain a typical particle velocity of about one.

4.1. Error Reduction Factors

TABLE I

Error-Reduction Factors Exhibited by the Implicit Solver with Distributive Relaxation and Perturbed-Modon Initialization

Cycle	R'	B'	$\mathscr{H}_{\min}$	$R\mathscr{P}_{\max}$	$\overline{\mu}_{\text{eff}}$
$V(1,1)$	0.10	0.97	0.895	1.23	0.26
$V(1,1)$	0.31	0.92	0.665	1.96	0.28
$V_4(1,1)$	0.31	0.92	0.665	1.96	0.26
$V(1,1)$	0.51	0.87	0.410	3.66	0.40
$W(1,1)$	0.51	0.87	0.410	3.66	0.29
$V_3(1,1)$	0.51	0.87	0.410	3.66	0.27
$V_2(1,1)$	0.51	0.87	0.410	3.66	0.26
$V_2(1,1)$	0.72	0.82	0.131	12.87	0.37
Bigrid(1,1)	0.72	0.82	0.131	12.87	0.37

Note. $V_l(1,1)$ denotes a V cycle with one pre-relaxation sweep and one post-relaxation sweep on the l finest levels, but two pre-sweeps and two post-sweeps on all coarser levels.

implicit solver appear in Table I. The explicit solver yields an error-reduction factor of 0.26 with the usual $V(1,1)$ cycle for all the cases appearing in Table I.

Normally, one $V(1,1)$ cycle per refinement will suffice to reduce the algebraic error well below truncation level if $\overline{\mu}_{\text{eff}}$ is about 0.3 or less (see discussion in [3, sect. 7]), but this must be tested experimentally. In particular, if there are excessive high-frequency and high-wavenumber components in the solution, more work may be required. But such components are often an indication of nonlinear instability [21] and they cannot be accurately resolved anyway.

The results shown in Table I indicate that regular $V(1,1)$ cycles should suffice when R' is small or moderate. When R' is larger, smoothing is adversely affected on all grids for which $B'\mathscr{H}_{\min}$ is of the order of the square of the mesh-size, as predicted by the coupling analysis (see Section 3.4). More work must then be performed on the coarse grids. But, since the problem is just the smoothing on the coarse grids and not the quality of the coarse-grid correction itself, one need not resort to W cycles (i.e., perform more cycles on the coarse grids) but rather perform more relaxation sweeps on coarse grids. This is less costly and more effective, as seen in Table 1. The increase in cost incurred by employing the V_l cycle, compared to the V cycle, is just 4^{-l} times the work spent only on the relaxation part in the V cycle, whereas a W cycle costs 50% more than a V cycle.

When R'/B' is large enough that the minimal water-height is reduced by about an order of magnitude, the $V_2(1,1)$ cycle yields an error-reduction factor of 0.37. But the corresponding bigrid cycle (i.e., a correction cycle in which the problem on the second-finest grid was solved well, using many cycles) does no better, indicating that the fine-grid smoothing is already adversely affected by the coupling of the equations. At this point one needs to apply more smoothing on the fine grids as well (e.g., a $V(2,1)$ cycle).

4.2. *Long-Time Integration: Modons*

We performed many numerical tests by integrating modons over long periods of time, and we present here typical examples. The time-steps are chosen adaptively at each time-level, in order to maintain an approximately constant Courant number throughout the calculation (except at the last time-step, which is adjusted to yield the desired total time of integration). The total integration time is 32 in all these experiments, which, given that the typical particle velocity is about one, implies approximately fifteen eddy recirculations. Shown in the figures are vorticity contours, shifted back by the distance that an exact modon (satisfying the differential equations with vanishing R on an infinite domain) will have traveled, i.e., by $c \cdot t$, where $t = 32$ is the total time of integration and $c = 0.1$ is the theoretical propagation velocity.

In all the figures depicting vorticity contours the contour interval is 1, and the contours are staggered (spanning the zero contour for clarity). Figure 1a shows vorticity contours of the modon at $t = 0$. Figures 1b and 1c depict the vorticity contours of the modon at the end of the integration with the explicit and implicit solvers, respectively, at $R = 0$. Both results are accurate, both in terms of the shape of the modon and the propagation speed. The results are obtained with $C = 1$, employing the 1-F cycle with $V(1,1)$ correction cycles. These calculations are repeated with Courant numbers 10, 20 and 40. At $C = 10$ the same algorithm as above is used, but the first equation is relaxed four times per each relaxation of the other equations, since smoothing of the advection operator deteriorates with increasing C. The calculations with the larger Courant numbers are carried out with two and three $V(2,2)$ cycles, respectively, which are more than necessary, the object being to examine the accuracy, rather than efficiency, at large time-steps. Figure 1d shows the vorticity contours at the end of the calculation with $C = 40$. The results are seen to be fairly accurate even at quite large time-steps. The reason for this appears to be that the rate of change of the flow pattern (0.1) is small compared to the maximal particle velocity (about 1). This phenomenon is strongly influenced by B', the velocities becoming comparable when B' is large (see also below). Also, the modons represent an extreme situation, where the solution is steady in a moving framework. For the most general advection problem it is well-known that one cannot greatly exceed Courant number without loss of accuracy. Hence, the degree to which large time-steps can be used depends on the physical properties of the flow.

Efficiency at large time-steps could be improved by applying such techniques as were developed in [6] for steady-state flows, but Courant numbers far greater than about 10 (for which such techniques are necessary) are unlikely to be desirable unless the flow-patterns evolve extremely slowly in time (see also Section 4.3).

Figure 2a shows solutions at $R' = 0.3$, where no uniformly

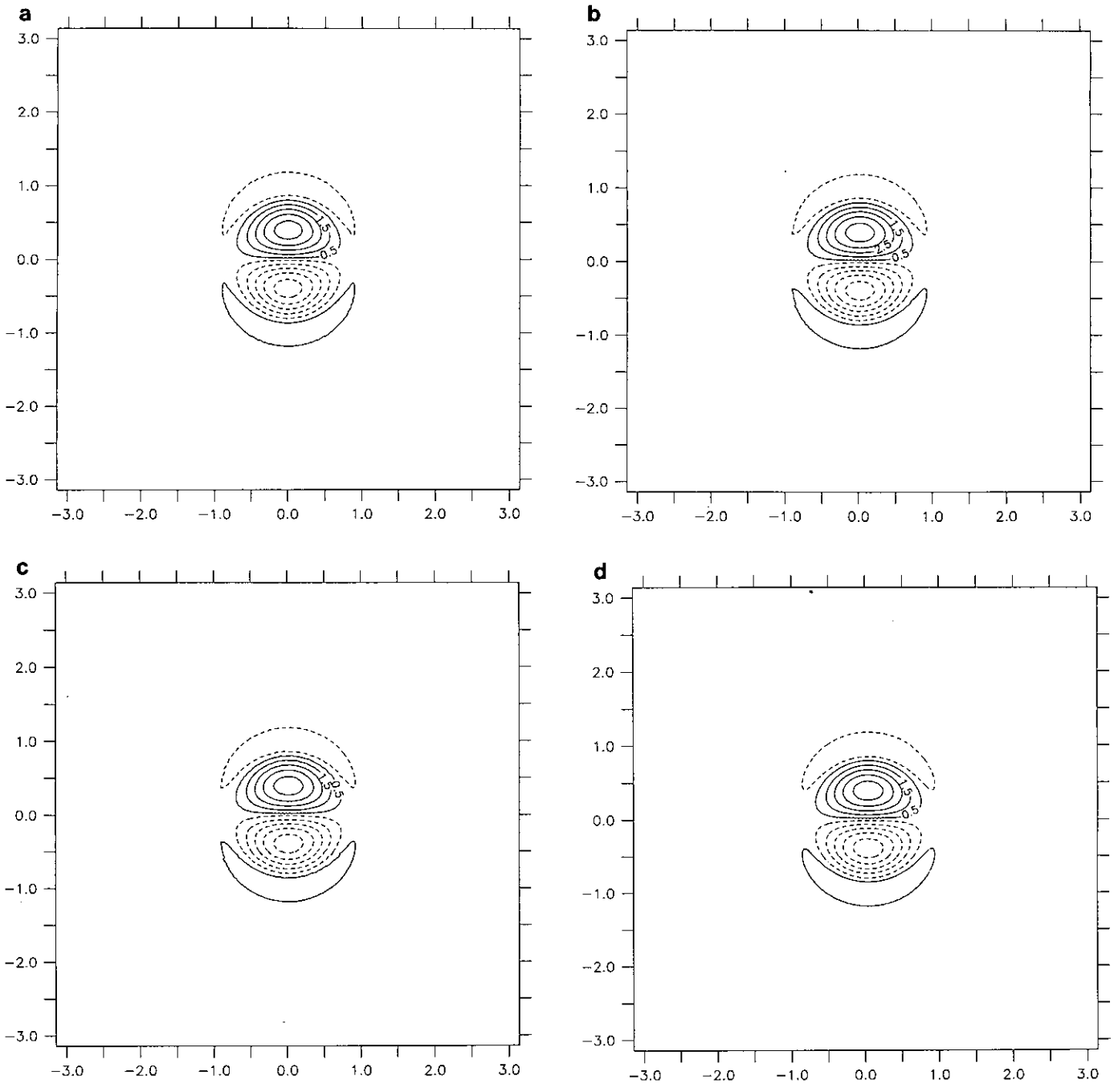

FIG. 1. Vorticity contours of modon at $t = 0$ (a) and $t = 32$ (b, c, d) with $R' = \nu = 0$. (b) and (c) show the solution of the explicit and implicit solvers, respectively, with $C = 1$. (d) shows the solution of the implicit solver with $C = 40$.

propagating solutions are known. Note in 2a and 2b that there are slight differences in fine-scale phenomena (which are not resolved well on the grid), due to the differing temporal discretizations. Figures 2c and 2d show results of the same calculation, employing the explicit solver, with $C = 1.4$ and 1.5, respectively. Clearly, the linear stability analysis, which predicts the point of instability to be $\sqrt{2}$, is quite accurate here. Figure 3 shows the results of the same calculation employing the implicit solver but with a biharmonic diffusivity $\nu = 6.25 \times 10^{-8}$. This small viscosity suffices to dissipate the small-scale vorticity generated by a weak nonlinear cascade with virtually no effect on large-scale phenomena. Note, in particular, that the total distance traveled by the modon and the extremal vorticity-values are virtually unaffected; see also Table 2 below. The same cycles as in the $R =$

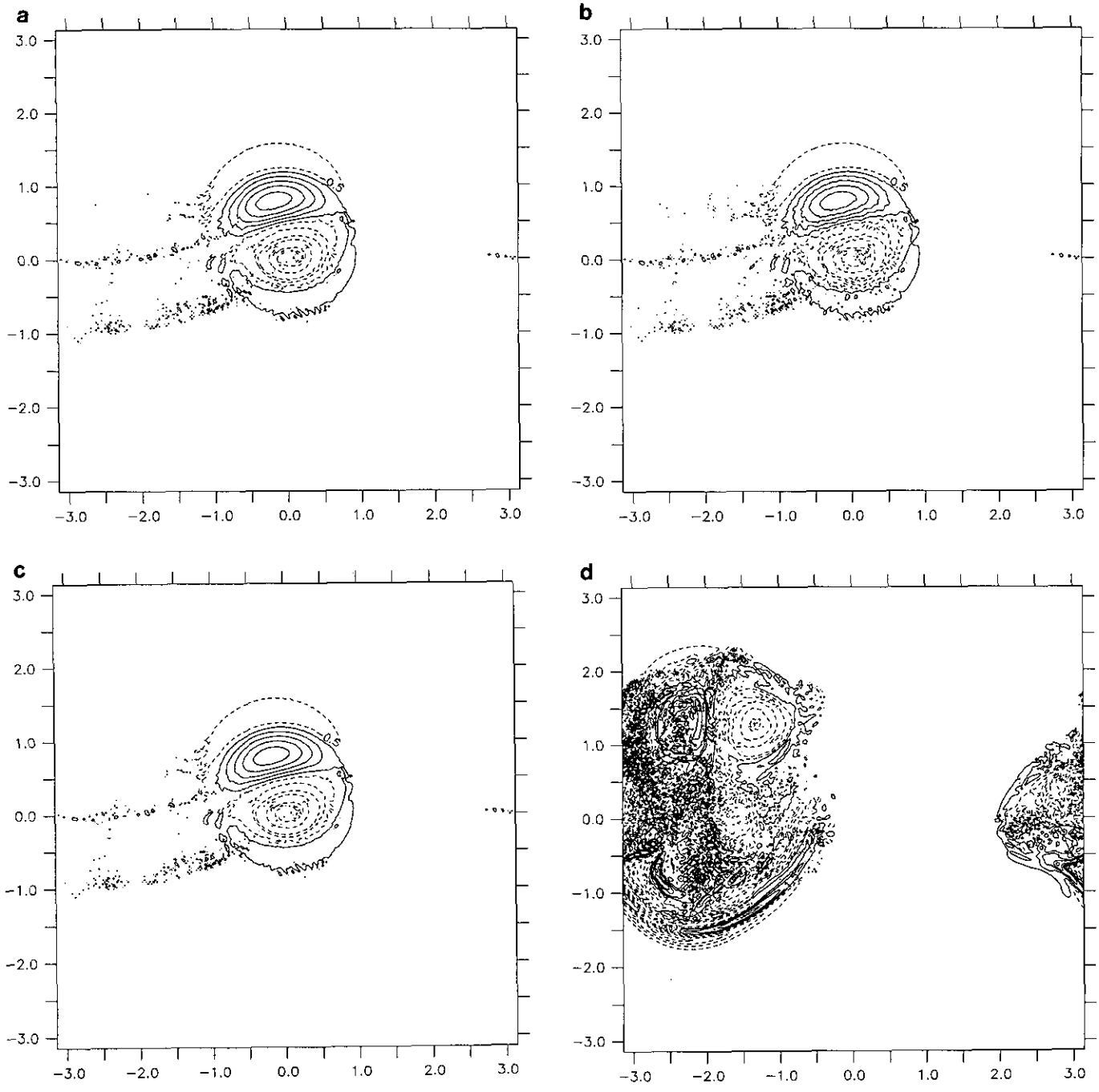

FIG. 2. Vorticity contours of modon at $t = 32$, with $R' = 0.3$ and $\nu = 0$. (a) and (b) show $C = 1$ solutions of the explicit and implicit solvers, respectively. (c) and (d) show the solutions of the explicit solver with $C = 1.4$ and $C = 1.5$, respectively.

0 case described above are used, and here too discernible loss of accuracy occurs only at quite large time-steps.

The potential vorticity $\mathcal{P}$ in the solution to the differential equations is conserved along trajectories when $\nu = 0$. In particular, the maximal and minimal values of $\mathcal{P}$ should remain constant in time in the inviscid case, and they can be used as an accuracy measure. Similarly, the spatial average of the potential enstrophy $\mathcal{H}P^2$ should remain invariant in time when $\nu = 0$, and it too can be used as a measure of accuracy. To avoid obscuring the errors due to smallness of the significant values, we define

$$\hat{\mathcal{P}} = \begin{cases} \mathcal{P} - R^{-1}, & R > 0 \\ \zeta - \phi/B, & R = 0 \end{cases} \tag{62}$$

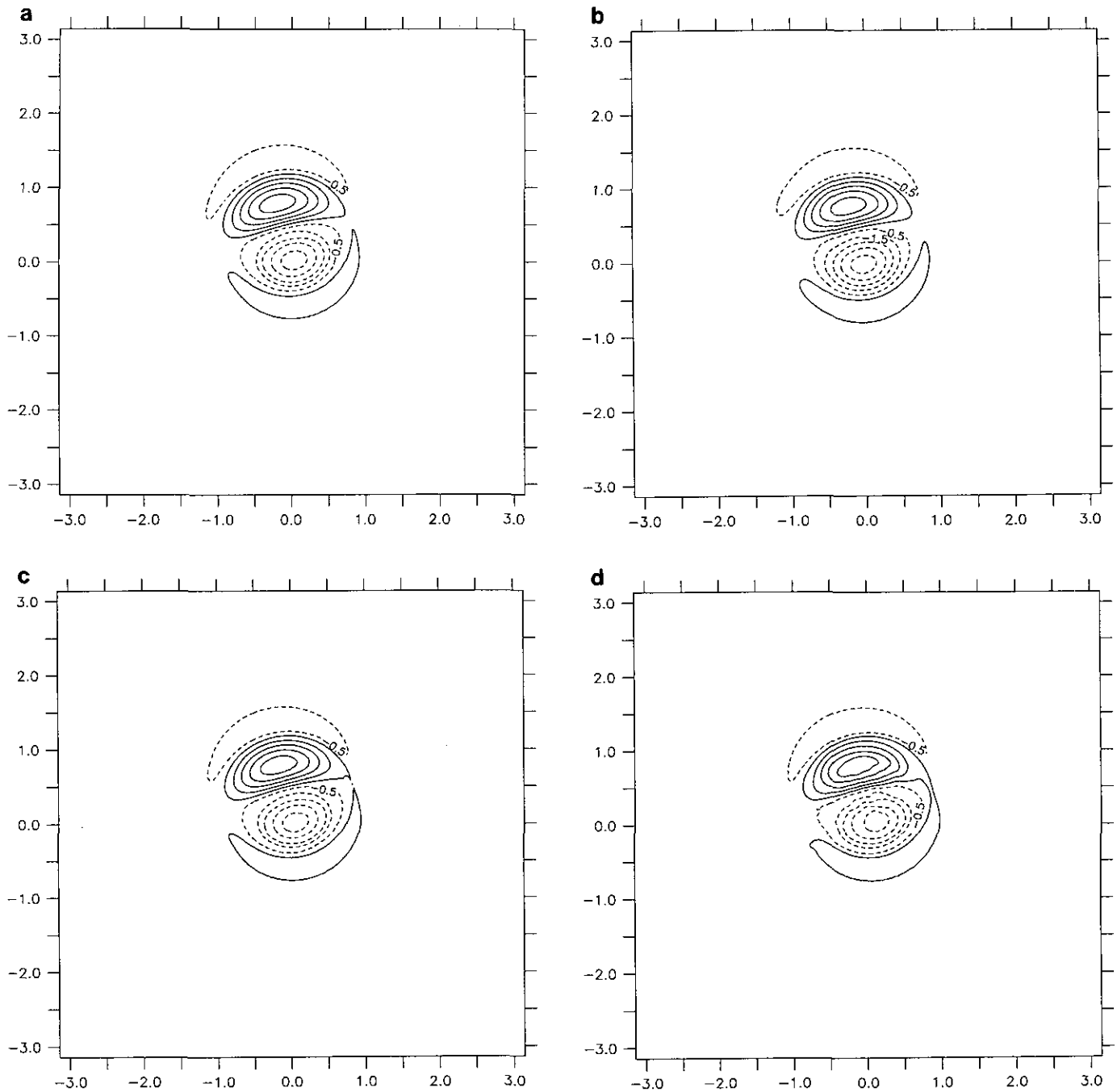

FIG. 3. Vorticity contours of modon at $t = 32$, with $R' = 0.3$ and $\nu = 6.25 \times 10^{-8}$, calculated with the implicit solver. The Courant numbers are 1 (a), 10 (b), 20 (c), and 40 (d).

$$\hat{PE} = \begin{cases} \langle \mathcal{H}(\mathcal{P} - R^{-1})^2 \rangle, & R > 0 \\ \langle (\zeta - \phi/B)^2 \rangle, & R = 0 \end{cases} \tag{63}$$

These invariants, calculated at $t = 32$ and normalized by dividing by the corresponding values at $t = 0$, appear in Table II for various cases. The extremal values of the potential vorticity are maintained well at vanishing Rossby number for all time-steps used. At $R' = 0.3$ an error of about 5% develops in these values, which improves somewhat (for the minimal value) when small viscosity is added. Once more, there is no significant loss in accuracy when the time-steps are increased. Although there appears to be some loss in accuracy with respect to the average potential-enstrophy conservation with increased time-steps, it is slight. At $R' = 0.3$ the average potential enstrophy decreases by about 1% in the inviscid case. Adding viscosity decreases this value still more, by dissipating the evolving high-wavenumber components.

TABLE II

Modon Potential Vorticity and Enstrophy at $t = 32$, Normalized by the Initial Values

Solver	Grid	R'	C	ν	$\frac{\hat{\mathcal{P}}_{min}(32)}{\hat{\mathcal{P}}_{min}(0)}$	$\frac{\hat{\mathcal{P}}_{max}(32)}{\hat{\mathcal{P}}_{max}(0)}$	$\frac{\hat{PE}(32)}{\hat{PE}(0)}$
Explicit	256^2	0	1	0	1.0059	1.0059	1.0001
Implicit	256^2	0	1	0	1.0060	1.0060	1.0001
Implicit	256^2	0	10	0	1.0062	1.0063	1.0006
Implicit	256^2	0	20	0	1.0040	1.0040	1.0016
Implicit	256^2	0	40	0	1.0071	1.0072	1.0027
Implicit	128^2	0	0.5	0	1.0353	1.0353	1.0031
Explicit	256^2	0.3	1	0	1.063	0.948	0.9885
Implicit	256^2	0.3	1	0	1.065	0.948	0.9896
Implicit	128^2	0.3	0.5	0	1.096	0.777	0.9649
Implicit	256^2	0.3	1	6.25×10^{-8}	1.008	0.948	0.9809
Implicit	256^2	0.3	10	6.25×10^{-8}	1.004	0.947	0.9715
Implicit	256^2	0.3	20	6.25×10^{-8}	1.012	0.949	0.9832
Implicit	256^2	0.3	40	6.25×10^{-8}	1.021	0.949	0.9913
Implicit	128^2	0.3	0.5	1×10^{-6}	1.024	0.804	0.9272

In all cases, even at $C = 40$, results obtained on the 256^2 grid are more accurate than those obtained on a twice-coarser grid at $C = 0.5$ (i.e., employing the same time-steps as in the fine-grid solution at $C = 1$). This, and the fact that the results of the implicit solver match those of the explicit solver, suggest that the solvers are indeed yielding essentially as good a solution as the spatial discretization and resolution allow. In the viscous solutions the coarse-grid biharmonic-viscosity is sixteen times as large as on the fine-grid, since the wavenumbers that need to be diffused are twice as large and therefore their fourth derivatives are sixteen times as small (see also below).

4.3. *Long-Time Integration: Turbulence*

The performance of the implicit solver is also tested on decaying turbulent flow. We initialize with a narrow-band, low-wavenumber, random-phase vorticity field and integrate from $t = 0$ to $t = 75$. Again, the initial vorticity is normalized so that a typical velocity of about one is obtained. The typical spatial scales are initially somewhat smaller than those of the modons of Section 4.2 to yield sufficiently reliable statistical measures of the flow; Figure 4 shows the initial vorticity field in all the calculations reported here. The development of the flow and the performance of the solver are tracked by monitoring the normalized potential enstrophy $\hat{PE}$ and extremal values of the potential vorticity $\hat{\mathcal{P}}$ (see Section 4.2) and also the vorticity kurtosis, $\langle\zeta^4\rangle/\langle\zeta^2\rangle^2$. In addition to monitoring the potential enstrophy as a function of time, we also calculate the integral over time of the dissipated enstrophy. By (31–33), this is given by $2\int_0^t \langle \nu\mathcal{P}\cdot\mathcal{D}A\rangle\, d\tau$, and its sum with the remaining spatially-averaged potential enstrophy is constant in time in the exact solution to the differential equations. Fourth-order time integration was used in this diagnostic calculation, so as not to add errors that are comparable to the solution errors being tested.

The physical expectation is that enstrophy will be dissipated through a cascade towards small scales, and, after the emergence of coherent vortices, the dissipation rate will weaken, extrema in $\hat{\mathcal{P}}$ will be approximately preserved within surviving vortices, and the kurtosis will increase as an indication of increasing spatial intermittency [19]. Furthermore, from Quasi-geostrophic Shallow-Water solutions we expect that the evolutionary rates for all these behaviors will decrease strongly as B decreases [16]. The amount of biharmonic diffusivity is determined by requiring sufficient smoothness in these properties, the vorticity contours, and the spectrum of the vorticity. As anticipated, it was found that the viscosity coefficient required on a 128^2 grid is about sixteen times as large as that required on a 256^2 grid.

We present here the results of four representative cases:

1. $B' \approx 5$, $R' = 0$.
2. $B' \approx 5$, $R' \approx 2.5$.
3. $B' \approx 10^5$, $R' = 0$ (the two-dimensional limit).
4. $B' \approx 1$, $R' = 0$ (the Quasigeostrophic limit).

The values of B' are chosen so as to span the relevant geophysical regimes for large-scale motions in the ocean and atmosphere, ranging from ones with dominant scales of motion comparable to the deformation radius (case 4), to others where it is very much smaller (case 3).

The B' and R' values are approximate, since B and R are fixed in time, while the minimal values of ϕ and ζ vary. However, we found that the evolution of these parameters was never so great as to change the regimes under consideration. Also, B is the same in problems 1 and 2, and therefore the B', which depends on R through ϕ is slightly different. Note that, by the definition of R', conditions (24) and (25) are severely violated in problem 2. The calculations are performed at both a moderate Courant number, $C = 2$, and also at a larger Courant number, $C = 5$ for problems 1–3 and $C = 10$ for problem 4. When $C = 5$ two relaxation sweeps of the equation for ζ are performed per each sweep of the system, and when $C = 10$ four such sweeps are performed. The extra sweeps are necessary due to the loss of smoothing efficiency of the advection operator at large Courant numbers. In all the calculations the viscosity coefficient is chosen to be $\nu = 8 \times 10^{-7}$. This value is roughly the minimum viscosity required for the high-B flow, and it can be reduced somewhat for moderate B, where the cascade and dissipation rates are smaller (see below).

Figures 5 and 6 show the vorticity-contours at late times. 5a and 5b depict the results of problem 1 at moderate and large Courant number, respectively, and 5c and 5d show the results of problem 2. Even at this late time ($t = 50$) there is a fair degree of pointwise correlation between the moderate and large Courant number solutions for each problem. The flows in the two problems appear to have evolved at about the same rate, as measured, for example, by the number of remaining vortices. The striking difference between the solutions is the dominance


3.0

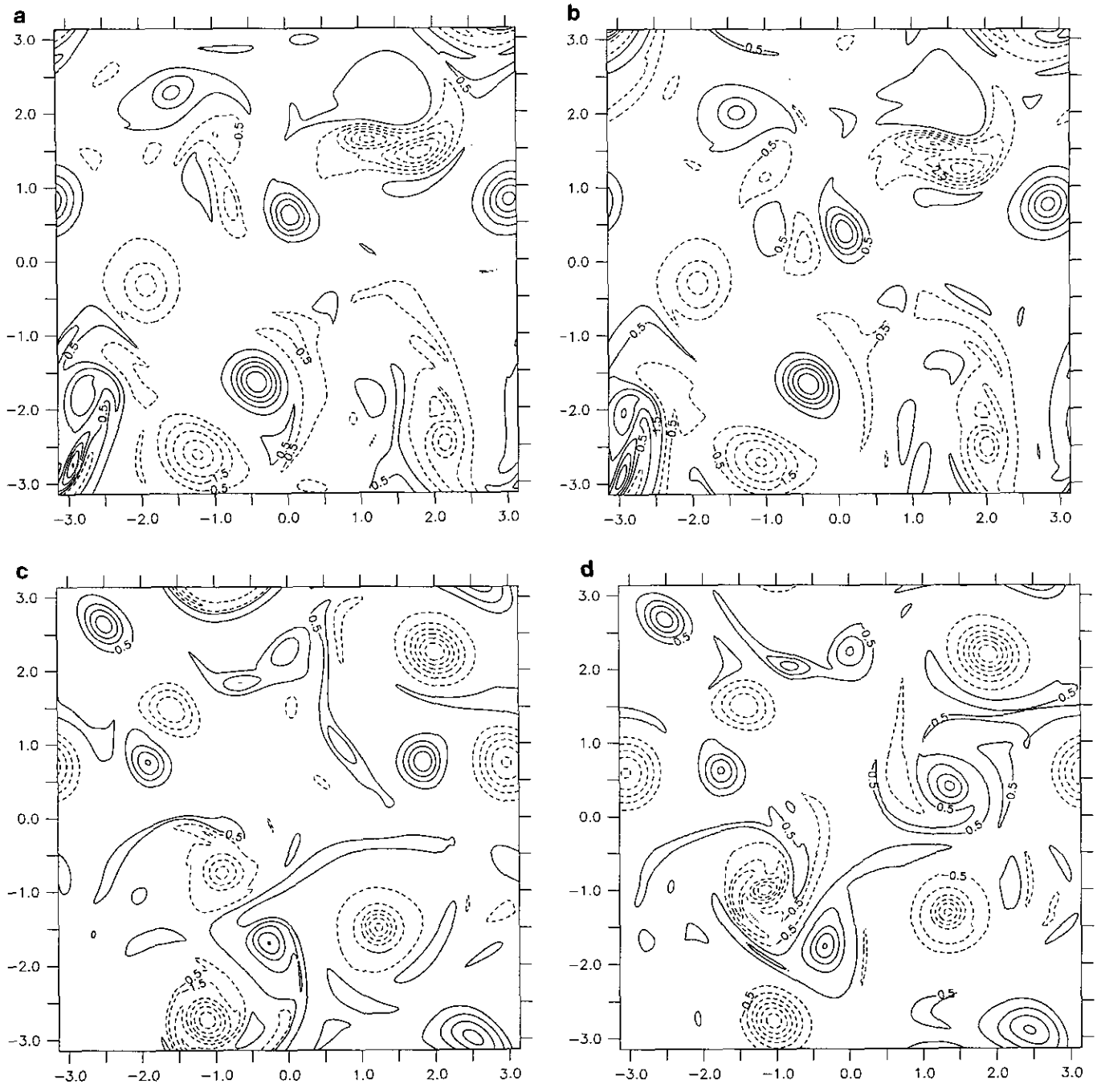

FIG. 5. (a) $B' \approx 5$, $R' = 0$, $C = 2$; (b) $B \approx 5$, $R' = 0$, $C = 5$; (c) $B' \approx 5$, $R' = 2.5$, $C = 2$; (d) $B' \approx 5$, $R' = 2.5$, $C = 5$. Vorticity contours of turbulence simulations at $t = 50$.

grows at a quicker rate when B is large. It is somewhat sensitive to phase decorrelation, since the total number of coherent vortices within the domain is not large enough to make the statistical sampling variability small, especially at late times. Thus, the large-C solutions are seen to depart from the moderate-C solutions at some point. Here too, the large-C solution is seen to be very accurate when B is about one and less accurate for larger B. Figure 8b depicts the skewness of the probability distribution function of the vorticity, $\langle \zeta^3 \rangle / \langle \zeta^2 \rangle^{3/2}$, sampled at times 0, 10, 25, 50, and 75. The skewness is expected to be zero due to the $R = 0$ or $B = \infty$ symmetry, except for sampling variability. But when R is large, a significant bias towards negative skewness is exhibited; this is a measure of the anticyclonic vortex dominance described above.

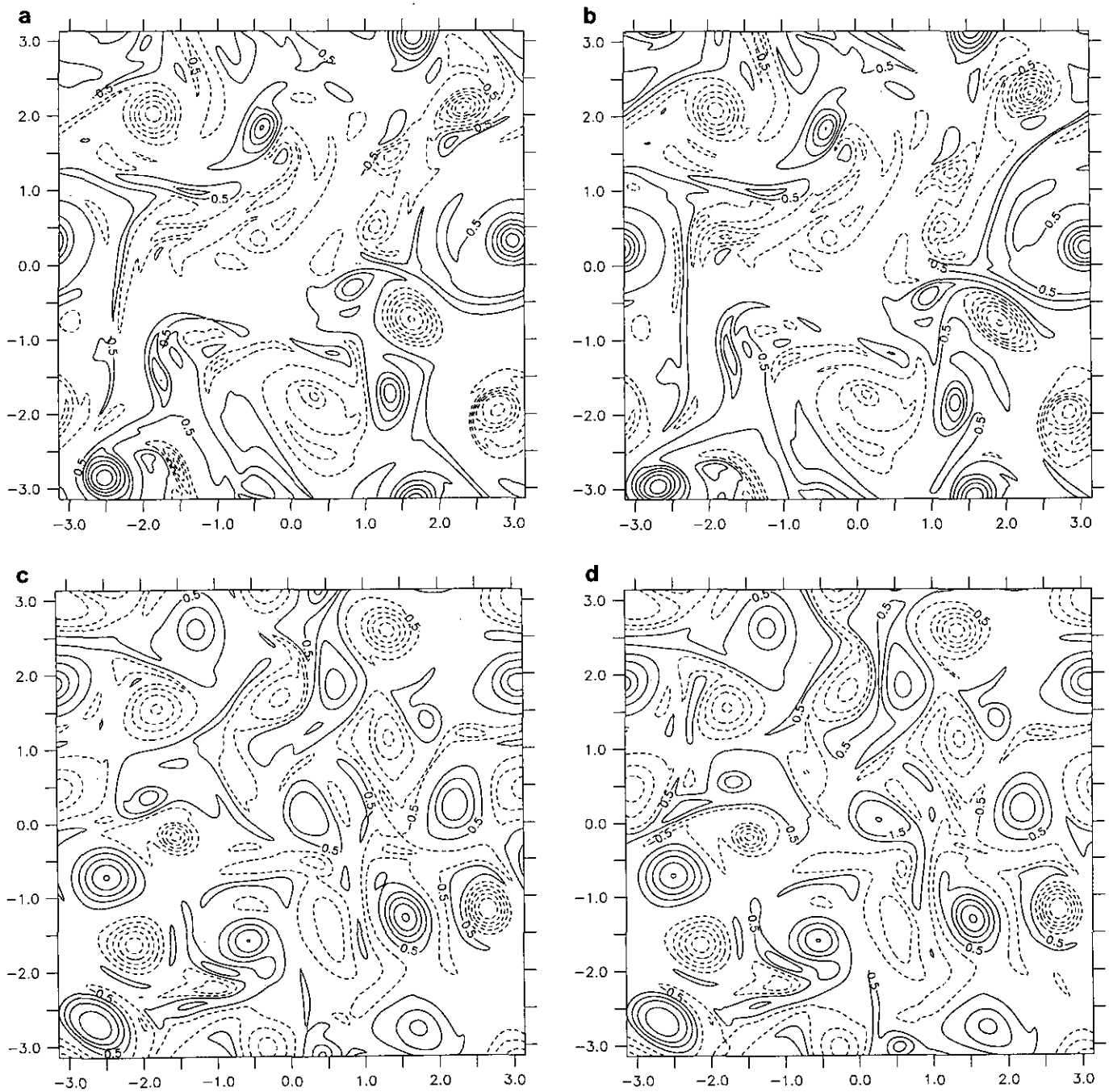

FIG. 6. (a) $B' \approx 10^5$, $R' = 0$, $C = 2$; (b) $B' \approx 10^5$, $R' = 0$, $C = 5$; (c) $B' \approx 1$, $R' = 0$, $C = 2$; (d) $B' \approx 1$, $R' = 0$, $C = 10$. Vorticity contours of turbulence simulations at $t = 25$ (a, b), and $t = 50$ (c, d).

Figure 9 shows the extremal values of the potential vorticity as a function of time. In most instances the extrema exhibit only a slow decline due to the weak diffusion, insofar as surviving coherent vortices experience little deformation and dissipation in their core. Deviations from this behavior that show increases in amplitude on a short time scale are indicative of numerical error. Large-C behavior is seen to be good by this criterion. Case 2, with its large R (Fig. 9b), exhibits sudden drops in its maximal potential vorticity, which we believe to be related to the preferential weakening and destruction of cyclonic vortices with positive vorticity, as also seen in Figs. 5c, 5d, and 8b.

5. SUMMARY AND FUTURE RESEARCH

Integration of the Shallow-Water Balance Equations has been shown to involve solution of an elliptic system of equations,

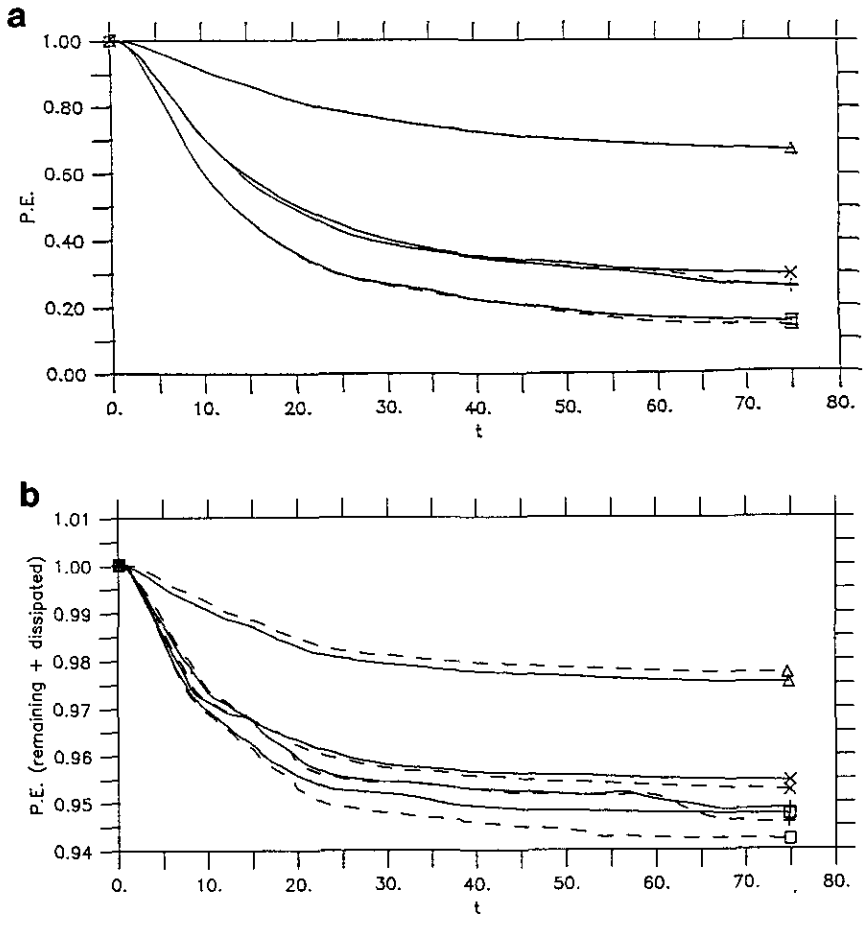

FIG. 7. (×) $B' \approx 5$, $R' = 0$; (+) $B' \approx 5$, $R' = 2.5$; (□) $B' = 10^5$, $R' = 0$; (△) $B' \approx 1$, $R' = 0$. Spatially averaged, normalized potential enstrophy as a function of time (a), and the sum of the spatially averaged remaining and calculated dissipated potential enstrophy as a function of time (b). Solid lines correspond to $C = 2$, and dashed lines to large Courant number solutions.

even when explicit time-stepping is used. This system can be written as a sum of a constant-coefficient system, which is efficiently invertible by direct methods for simple enough domains, and a non-constant part which is proportional to ε. When ε is small, previously employed methods of iteration, whereby the non-constant part is updated only at the end of each iteration, are efficient. But when ε is larger these methods rapidly lose their efficiency and eventually fail.

The efficiency of the multigrid solvers developed here is not unduly affected by non-constant coefficients. Also, the elliptic nature of the problem that is solved at each time level assures good behavior on fine grids. When ε becomes large, more coarse-grid work may be required, but the extra cost involved is small. In extreme cases one might expect to require specialized methods for indefinite problems on the coarse grids. While these are computationally prohibitive in the single-grid context, they can be used in the multigrid framework, as they would only be needed on coarse grids. When ε is small enough that only a few iterations are required by existing solvers, the solvers developed here are comparatively less efficient, but they can be modified straightforwardly to yield the same efficiency.

The implicit solver developed is less costly per time-step than the explicit solver, and it is also unrestricted by CFL stability constraints. The latter property has been found to be important, inasmuch as large time-steps can be taken while retaining a high degree of accuracy in problems where the radius of deformation $r_d = \sqrt{B'}$ is not large. This is explained by the fact that the effect of a point vortex on the velocities at distance r is asymptotically proportional to $\exp(-r/r_d)$ for finite r_d, but to $1/r$ for infinite r_d (i.e., two-dimensional flow). As a result, the intermediate- and large-scale flow patterns change quite slowly compared to the typical particle velocities when r_d is moderate. This property cannot be exploited by semi-Lagrangian schemes, for example, since they follow the trajectories rather than the patterns.

We have not considered the treatment of boundaries in this work. However, there is a great deal of analytical and experimental evidence that shows that multigrid efficiency for elliptic problems is unaffected by boundaries and boundary conditions, at the cost, perhaps, of extra processing along the boundaries, which becomes negligible as the mesh-size becomes small (see, e.g., [29, sect. 2] for numerical results with the Stokes system,

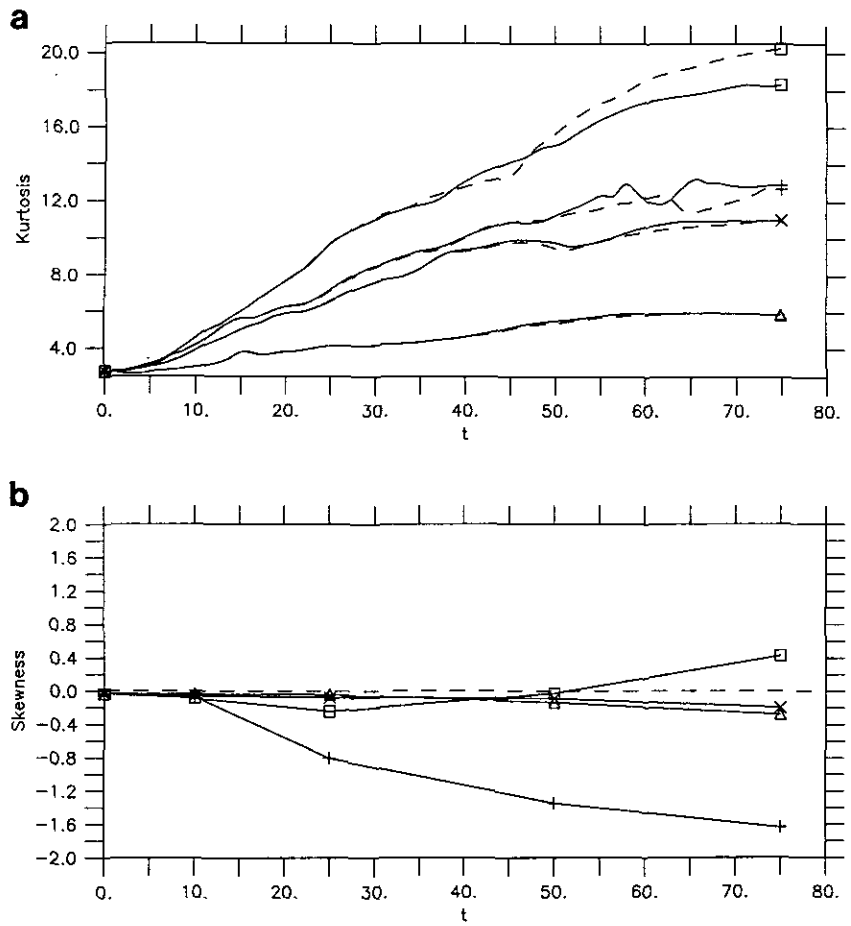

FIG. 8. (×) $B' \approx 5$, $R' = 0$; (+) $B' \approx 5$, $R' = 2.5$; (□) $B' = 10^5$, $R' = 0$; (△) $B' \approx 1$, $R' = 0$. Kurtosis (a) and skewness of vorticity (b) as a function of time. In (a) solid lines correspond to $C = 2$, and dashed lines to large Courant number solutions. In (b) the dashed line is at 0 skewness for reference.

and [4] for general analysis). In the relevant sense the system solved at each step of the implicit solution algorithm, as well as the explicit algorithm, is elliptic.

In developing the solvers we have employed the coupling analysis introduced in [28]. This has been found to be a very useful tool, and its predictions match well the results of numerical tests of asymptotic error-reduction factors. We have also developed a fully-implicit solver for the Shallow-Water Equations, which we have used in researching the limits of the slow manifold [30]. This research required integration of the SWBE at near-singular conditions of nearly-vanishing water height. The present implicit solver was used, and it exhibited a high degree of robustness in these calculations. Presently, we are developing parallel multigrid solvers for the three-dimensional balance equations, based in part on the present techniques, which will be used in high-resolution long-time integration.

APPENDIX

Here are the coupling analyses for the systems (18) and (36) and the corresponding transformed systems (49) and (53). A comprehensive description of the theory and application of the coupling analysis appears in [28].

For (18) the order-array Q, whose elements are the corresponding orders of the operators in the left-hand side of (18), and the weight-array W, whose off-diagonal elements are the difference between the corresponding elements in Q and the Q diagonal elements of the same columns, are given by

$$Q = \begin{bmatrix} 2 & 0 & N \\ N & 2 & 2 \\ 2 & N & 2 \end{bmatrix}, \qquad W = \begin{bmatrix} N & 2 & N \\ N & N & 0 \\ 0 & N & N \end{bmatrix}.$$

Here, N is the null symbol. The coefficient-array C, calculated after dividing the first equation through by the coefficient of its principal diagonal term, is given by

$$C = \begin{bmatrix} 1 & [1, B]/B\mathcal{H} & N \\ N & 1 & 1 \\ \varepsilon\mathcal{A} & N & 1 \end{bmatrix}.$$

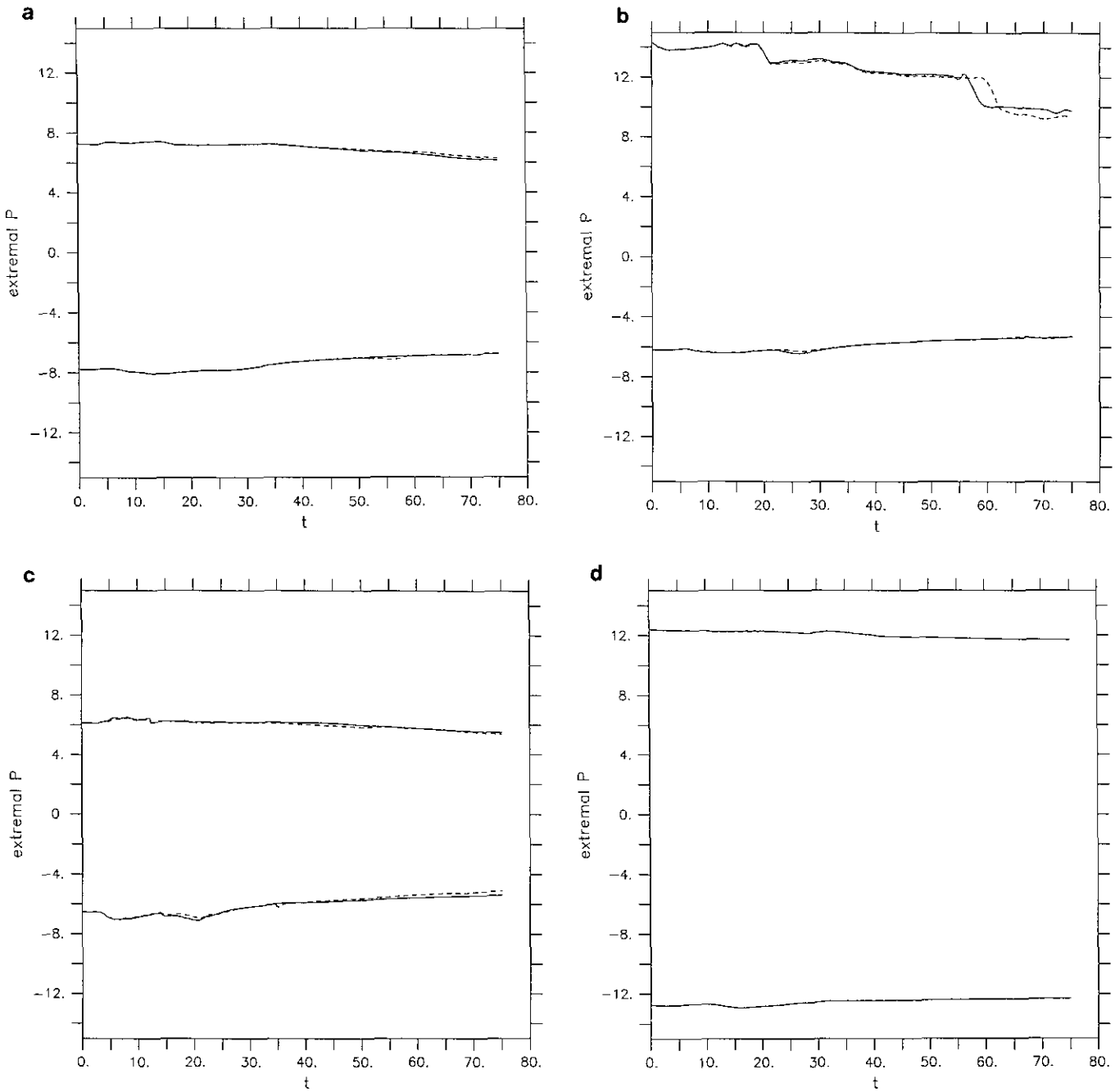

FIG. 9. (a) $B' \approx 5$, $R' = 0$; (b) $B \approx 5$, $R' = 2.5$; (c) $B' \approx 10^5$, $R' = 0$; (d) $B' \approx 1$, $R' = 0$. Extremal values of potential vorticity as a function of time. Dashed lines depict large Courant number solutions.

The coupling graph is plotted in Fig. 10a. There is a single loop, whose weight-sum is two, and whose coefficient-product is $R\mathcal{P}[1, R]/B$. This implies the first term in condition (46). (The $\frac{1}{3}$ power is due to the multiplicity of the Laplace operator, which is relaxed in each of the three equations appearing in the loop.) The second term in (46) is due to the non-principal term in $L_{\mathcal{H}}$.

In order to apply the coupling analysis to (36), we must first choose the correct one-to-one correspondence between equations and unknowns; i.e., we must decide which unknown to relax in each equation. Hence, we construct Q for some arbitrary tentative choice, and permute the rows so as to maximize the trace (treating N as $-\infty$). The resulting order-array Q, written below, implies that the first equation be relaxed for ζ, the second for χ, the third for ϕ and the fourth equation for ψ. This choice is determined from the elements on the diagonal of Q. The order-array and weight-array for (36), when ν is at most of the order of the

mesh-size (greater values of ν yield weaker coupling), are given by

$$Q = \begin{bmatrix} 1 & 2 & N & 1 \\ N & 2 & 1 & 1 \\ N & N & 2 & 2 \\ 0 & N & N & 2 \end{bmatrix}, \qquad W = \begin{bmatrix} N & 0 & N & 1 \\ N & N & 1 & 1 \\ N & N & N & 0 \\ 1 & N & N & N \end{bmatrix}.$$

The coefficient-array is

$$C = \begin{bmatrix} 1 & \varepsilon\mathcal{A}\alpha & N & \alpha \\ N & 1 & [1,B]/B\mathcal{H}\alpha & [1,B]/B\mathcal{H} \\ N & N & 1 & 1 \\ 1 & N & N & 1 \end{bmatrix}.$$

The coupling graph is plotted in Fig. 10b. There are three loops: (1,4,1), which implies the first term in (47), (1,4,2,1), which implies the second term, and (1,4,3,2,1), which yields the third term in (47). The fourth term in (47) is again due to the non-principal part of the operator which operates on the relaxed variable χ in the second equation.

Q, W and C for (49) are given by

$$Q = \begin{bmatrix} 2 & 0 & N \\ 2 & 2 & 2 \\ 1 & N & 2 \end{bmatrix}, \qquad W = \begin{bmatrix} N & 2 & N \\ 0 & N & 0 \\ 1 & N & N \end{bmatrix},$$

and

$$C = \begin{bmatrix} 1 & [1,B]/B\mathcal{H} & N \\ \varepsilon\mathcal{A}R/[1,R] & 1 & 1 \\ \varepsilon & N & 1 \end{bmatrix}.$$

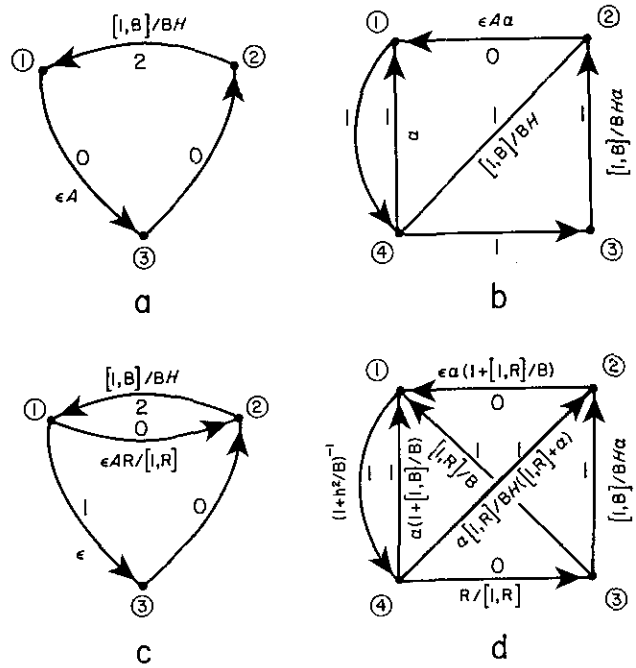

FIG. 10. Coupling graphs for a (18), b (36), c (49), d (53).

The coupling graph appears in Fig. 10c. Now there are two loops, (1,2,1), which implies the first term in (50) and (1,3,2,1), which implies the second term. The final term is once again implied by the nonprincipal part of $L_{\mathcal{H}}$.

The order-array and weight-array for (53) are given by

$$Q = \begin{bmatrix} 1 & 2 & 1 & 1 \\ N & 2 & 1 & 1 \\ N & N & 2 & 2 \\ 0 & N & N & 2 \end{bmatrix}, \qquad W = \begin{bmatrix} N & 0 & 1 & 1 \\ N & N & 1 & 1 \\ N & N & N & 0 \\ 1 & N & N & N \end{bmatrix}.$$

The coefficient-array is

$$C = \begin{bmatrix} 1 & \varepsilon(1 + [1,R]/B)\alpha & [1,R]/B & (1 + [1,R]/B)\alpha \\ N & 1 & [1,B]/B\mathcal{H}\alpha & [1,B]\alpha/B\mathcal{H}(\alpha + [1,R]) \\ N & N & 1 & R/[1,R] \\ 1/(1 + h^2/B) & N & N & 1 \end{bmatrix},$$

where we have included the non-principal part (which is relaxed) in the last equation, since we are specifically dealing also with the case where $B = O(h^2)$. The coupling graph for (53) appears in Fig. 10d, and the implied condition for weak coupling is (54).

REFERENCES

1. J. S. Allen, J. A. Barth, and P. A. Newberger, *J. Phys. Oceanogr.* **20,** 1949 (1990).
2. A. Brandt, *Math. Comput.* **31,** 333 (1977).
3. A. Brandt, "1984 Multigrid Guide with Applications to Fluid Dynamics,"

Monograph, GMD-Studies 85, GMD-FIT, Postfach 1240, D-5205, St. Augustin 1, West Germany (1985).

4. A. Brandt, Rigorous Local Mode Analysis of Multigrid, in *Prel. Proc. Fourth Copper Mountain Conference on Multigrid Methods,* (1989). Chap. 2.
5. A. Brandt and J. Greenwald, in *Multigrid Methods III,* edited by W. Hackbusch and U. Trottenberg. International Series of Numerical Mathematics, Vol. 98 (Birkhauser-Verlag, Basel, 1991), p. 143.
6. A. Brandt and I. Yavneh, *Siam J. Sci. Comput.* **14**(3), 607 (1993).
7. J. G. Charney, *Proc. Int. Symp. Numerical Weather Prediction,* (Meteor. Soc. Japan, Tokyo, 1962), p. 131.
8. R. Courant and D. Hilbert, *Methods of Mathematical Physics,* Vol. 2, (Interscience, New York/London, 1962).
9. B. Cushman-Roisin and B. Tang, in *Mesoscale/Synoptic Coherent Structures in Geophysical Turbulence,* edited by J. C. J. Nihoul and B. M. Jamart (Elsevier, Amsterdam, 1989), p. 51.
10. A. Douglis and L. Nirenberg, *Commun. Pure Appl. Math.* **8,** 503 (1955).
11. G. R. Flierl, V. D. Larichev, J. C. McWilliams, and G. M. Reznic, *Dyn. Atmos. Oceans* **5,** 1 (1980).
12. P. R. Gent and J. C. McWilliams, *Dyn. Atmos. Oceans* **7,** 67 (1983).
13. P. R. Gent and J. C. McWilliams, *Tellus* **36A,** 166 (1984).
14. J. M. Hyman, in *Nonlinear Problems: Present and Future,* (edited by A. R. Bishop, D. K. Campbell, and B. Nicolaenko, North Holland, Amsterdam, 1980), p. 91.
15. Y. Kurihara, *Mon. Weath. Rev.* **93,** 33 (1965).
16. V. D. Larichev and J. C. McWilliams, *Phys. Fluids A* **3,** 938 (1991).
17. E. N. Lorenz, *Tellus* **12,** 364 (1960).
18. J. C. McWilliams, *Dyn. Atmos. Oceans* **5,** 43 (1980).
19. J. C. McWilliams, *J. Fluid Mech.* **146,** 21 (1984).
20. N. J. Norton, J. C. McWilliams, and P. R. Gent, *J. Comput. Phys.* **67,** 439 (1986).
21. N. A. Phillips, *The Atmosphere and Sea in Motion,* Rockefeller Inst. Press, New York, 1959, p. 501.
22. L. M. Polvani, J. C. McWilliams, M. A. Spall, and R. Ford, "The Coherent Structures of Shallow-Water Turbulence: Deformation-Radius Effects, Cyclone/Anticyclone Asymmetry, and Gravity-Wave Generation," submitted for publication.
23. P. J. Roache, *Computational Fluid Dynamics* (Hermosa, Albuquerque, NM, 1976).
24. M. A. Spall and J. C. McWilliams, *Geo. Astr. Fluid Dyn.* **64,** 1 (1992).
25. S. Ta'asan, "Multigrid Methods for Slightly Indefinite Problems," Ph.D. Thesis (The Weizmann Institute of Science, Rehovot 76100, Israel, 1984).
26. K. Stüben and U. Trottenberg, in *Multigrid Methods,* edited by W. Hackbusch and U. Trottenberg (Springer-Verlag, Berlin, 1982), p. 1.
27. K. Tanabe, *Numer. Math.* **17,** 203 (1971).
28. I. Yavneh, *SIAM J. Sci. Comput.* **14**(6), 1437 (1993).
29. I. Yavneh, "Multigrid Techniques for Incompressible Flows," Ph.D. Thesis (The Weizmann Institute of Science, Rehovot, Israel), 1991.
30. I. Yavneh and J. C. Mcwilliams, "Breakdown of the Slow Manifold in the Shallow-Water Equations," *Geo. Astr. Fluid Dyn.* **75,** 131 (1994).